Self-similarity of the dipole–multipole transition in rapidly rotating dynamos

Debarshi Majumder[1], Binod Sreenivasan†[1], and Gaurav Maurya[1]

[1]Centre for Earth Sciences, Indian Institute of Science, Bengaluru 560012, India

(Received xx; revised xx; accepted xx)

The dipole–multipole transition in rapidly rotating dynamos is investigated through the analysis of forced magnetohydrodynamic waves in an unstably stratified fluid. The focus of this study is on the inertia-free limit applicable to planetary cores, where the Rossby number is small not only on the core depth but also on the length scale of columnar convection. By progressively increasing the buoyant forcing in a linear magnetoconvection model, the slow Magnetic-Archimedean-Coriolis (MAC) waves are significantly attenuated so that their kinetic helicity decreases to zero; the fast MAC wave helicity, on the other hand, is practically unaffected. In turn, polarity reversals in low-inertia spherical dynamos are shown to occur when the slow MAC waves disappear under strong forcing. Two dynamically similar regimes are identified – the suppression of slow waves in a strongly forced dynamo and the excitation of slow waves in a moderately forced dynamo starting from a small seed field. While the former regime results in polarity reversals, the latter regime produces the axial dipole from a chaotic multipolar state. For either polarity transition, a local Rayleigh number based on the mean wavenumber of the energy-containing scales bears the same linear relationship with the square of the peak magnetic field measured at the transition. The self-similarity of the dipole–multipole transition can place a constraint on the Rayleigh number for polarity reversals in the Earth.

1. Introduction

The dynamo operating in the Earth's outer core generates a predominantly North–South dipole magnetic field. Occasionally, the magnetic dipole axis flips its orientation and retains its approximate alignment with the Earth's rotation axis. The last such polarity reversal occurred nearly 0.78 million years ago (Merrill 2011). Geomagnetic excursions, the periods during which the magnetic axis wanders up to 45° from the rotation axis before returning to its original state, have been more frequent in the Earth's past. As reversals and excursions are likely to result from similar convective states of the core (Gubbins 1999; Valet *et al.* 2005), it is possible that the geodynamo operates for long periods in a state marginally below the threshold for reversals (Olson & Christensen 2006).

The first polarity reversals in numerical dynamo models were obtained by Glatzmaier & Roberts (1995*a*; 1995*b*). Since then, several other studies reported reversals in comparable parameter regimes (Sarson & Jones 1999; Kutzner & Christensen 2002; Wicht & Olson 2004; Olson *et al.* 2009; Sreenivasan *et al.* 2014), and it is now well accepted that dynamo reversals occur under strong buoyancy-driven convection. Any explanation for polarity reversals must follow from an explanation for the preference for the axial dipole in planetary dynamos. The kinetic helicity $\boldsymbol{u} \cdot \boldsymbol{\zeta}$ (where $\boldsymbol{u}$ is the velocity and $\boldsymbol{\zeta}$ is the vorticity) generated in convection columns that arise in rapid rotation is thought to be essential for dipolar dynamo action (Moffatt 1978; Olson *et al.* 1999; Sreenivasan & Jones 2011). Consequently, the loss of columnar helicity

---

† Email address for correspondence: bsreeni@iisc.ac.in

can lead to collapse of the dipole (e.g. Soderlund *et al.* 2012). A number of numerical dynamo models show a dipole–multipole transition for $Ro_\ell \approx 0.1$, where Ro_ℓ is a 'local' Rossby number that measures the ratio of nonlinear inertial to Coriolis forces on the length scale of columnar convection (Christensen & Aubert 2006). Since linear inertial waves are believed to sustain the columnar vortices in rotating turbulence (Davidson *et al.* 2006), the above polarity transition may result from the suppression of inertial waves in the dynamo above a critical value of Ro_ℓ (McDermott & Davidson 2019). Multipolar solutions may also be found when the ratio of nonlinear inertia to Lorentz forces exceeds a critical value (Zaire *et al.* 2022). That having been said, in the rapidly rotating limit of zero nonlinear inertia, the helicity of columnar vortices aligned with the rotation axis is considerably enhanced by the magnetic field in the dynamo (Sreenivasan & Jones 2011). It is thought that this field-induced helicity is essential for the formation of the axial dipole in planetary dynamos. Under strong buoyancy-driven convection, the magnetically enhanced columnar flow structures break down, leading to polarity reversals. Given the spatial inhomogeneity of the magnetic field, a global analysis of forces in the dynamo cannot possibly reveal how buoyancy offsets the Lorentz–Coriolis force balance in isolated columns. The analysis of helical dynamo waves at progressively increasing forcing can, on the other hand, provide an insight into the role of buoyancy in the loss of columnar helicity. This study aims to place a constraint on the convective state of the dynamo that admits reversals in the inertia-free limit, where the Rossby number is small not only on the depth of the planetary core but also on the columnar length scale transverse to the rotation axis.

In convectively-driven planetary cores, isolated density disturbances generate fast and slow Magnetic-Archimedean-Coriolis (MAC) waves under the combined influence of background rotation, magnetic field and unstable stratification. The fast waves are inertial waves weakly modified by the magnetic field and buoyancy while the slow waves are magnetostrophic waves produced by localized balances between the magnetic, Coriolis and buoyancy forces (Braginsky 1967; Busse *et al.* 2007). In rapidly rotating dynamos, the fast MAC waves of frequency $\sim \omega_C$, the frequency of linear inertial waves, exist in both weak and strong-field states. The intensity of slow MAC wave motions is comparable to that of the fast waves when the initial ratio of Alfvén to inertial wave frequencies,

$$\left(\frac{\omega_M}{\omega_C}\right)_0 \sim \frac{V_M}{2\Omega\delta} \sim 10^{-2}, \tag{1.1}$$

where V_M is the Alfvén wave velocity based on the peak magnetic field, Ω is the angular velocity of rotation, δ is the length scale of the buoyancy disturbance and the subscript '0' refers to the initial state of the disturbance as it is released into the flow (Varma & Sreenivasan 2022). Because of the anisotropy of the convection, the instantaneous value of ω_M/ω_C for parity between fast and slow wave motion would be higher than its initial value, and inferred to be ~ 0.1 from the spherical shell dynamo models of Varma & Sreenivasan. In the energy-containing scales, given by the range of spherical harmonic degrees greater than the mean value at energy injection, the kinetic helicity in the nonlinear dynamo is nearly twice than that in the hydrodynamic dynamo at the same parameters, where the Lorentz force is zero. This result implies that the helicity of the slow MAC wave motions in the nonlinear dynamo would be of the same magnitude as that of the inertial waves in the hydrodynamic dynamo. Since the hydrodynamic dynamo does not generate the axial dipole, we infer that the slow waves are essential for dipole formation. Although the magnetic diffusion frequency ω_η is the lowest frequency in the dynamo, small but finite magnetic diffusion can place a lower bound on the length scale that supports slow MAC waves in the energy-containing scales of the dynamo. Linear magnetoconvection analysis of a forced damped system (Sreenivasan & Maurya 2021) indicates that, for

$$\left(\frac{\omega_\eta}{\omega_C}\right)_0 \sim \frac{\eta}{2\Omega\delta^2} \lesssim 10^{-5}, \tag{1.2}$$

where η is the magnetic diffusivity, the energy of the fast and slow wave motions are comparable. (Here, $\omega_M/\omega_C \sim 0.1$). Therefore, slow wave motions at length scales $\sim$ 10 km can be influential in the generation of the dipole field. At higher E_η (defined in equation 2.25), the slow wave energy falls below the fast wave energy, implying that scales smaller than $\sim$ 10 km are rapidly damped by magnetic diffusion.

The role of buoyancy in a rapidly rotating dynamo is not merely in the excitation of MAC waves. In a convective dynamo that evolves from a small seed magnetic field, the slow MAC waves are first excited when $|\omega_M| > |\omega_A|$, where ω_A is a measure of the strength of buoyancy in an unstably stratified fluid and has the same magnitude as that of the frequency of internal gravity waves in a stably stratified fluid (Varma & Sreenivasan 2022). As the dynamo field intensity increases from its starting seed value, $|\omega_M|$ progressively increases and exceeds $|\omega_A|$, after which the axial dipole eventually forms from a chaotic multipolar state. Thus, the inequality $|\omega_C| > |\omega_M| > |\omega_A| > |\omega_\eta|$ represents a large region of the parameter space where dipole-dominated dynamos exist. If a rotating dynamo is subject to progressively increasing buoyant forcing, the larger self-generated fields would result in progressively larger ω_M until a state is reached where $|\omega_A| \sim |\omega_M|$ as the field attains its highest intensity for a given rotation rate. Here, the slow MAC waves disappear, likely causing collapse of the dipole. This transition from dipole to polarity-reversing states is dynamically similar to the transition from a multipolar state to the dipole that occurs in the growth phase of a dynamo starting from a seed field. Since ω_C remains the dominant frequency while forcing is increased, the dynamo reverses polarity in a rotationally dominant regime where slow magnetostrophic waves are suppressed. Although increased forcing may result in enhanced nonlinear inertia in numerical dynamo models, we consider it unlikely that inertia has any role in polarity transitions in the Earth even for the smallest buoyancy disturbances that support MAC waves. For disturbances of size $L_\perp \approx 15$ km transverse to the rotation axis, the actual ratio of nonlinear inertia to Coriolis forces,

$$\frac{|\nabla \times (\boldsymbol{u} \cdot \nabla)\boldsymbol{u}|}{|2(\boldsymbol{\Omega} \cdot \nabla)\boldsymbol{u}|} \sim \frac{u_\star L}{2\Omega L_\perp^2} \approx 0.03, \tag{1.3}$$

taking $L = 2260$ km and $u_\star = 5 \times 10^{-4}$ ms^{-1} (Starchenko & Jones 2002). Low-inertia numerical dynamos must have a small Rossby number based on the length scale of convection. The use of magnetic Prandtl number $Pm = \nu/\eta \sim 1$–10, where ν is the kinematic viscosity, is useful in realizing strong magnetic fields in numerical simulations (Willis *et al.* 2007; Teed *et al.* 2015; Dormy 2016) in the inertia-less regime relevant to rotating planetary cores. Although the choice of a large Pm at moderate Ekman number $E = \nu/2\Omega L^2 \sim 10^{-4}$–$10^{-6}$ has the unphysical consequence of the viscous dissipation being at least as high as the Ohmic dissipation, the advantage derived in terms of reproducing the MAC force balance in the energy-containing scales is crucial in the understanding of wave motions in both dipole-dominated and reversing regimes. The present study analyses polarity transitions in strongly driven, low-inertia dynamos.

In §2, we consider the evolution of a buoyancy disturbance in an unstably stratified rotating fluid subject to a magnetic field. In Cartesian geometry, the axes parallel to gravity, rotation and the magnetic field are chosen to be orthogonal to one another, which is a configuration relevant to planetary cores (Loper *et al.* 2003). At times much shorter than the time scale for exponential increase of the perturbation, the relative intensities of the fast and slow MAC wave motions generated by the perturbation are studied. Apart from the dipole-dominated regime given by $|\omega_C| > |\omega_M| > |\omega_A| > |\omega_\eta|$, the regime thought to be relevant to polarity transitions, $|\omega_C| > |\omega_M| \sim |\omega_A| > |\omega_\eta|$, is analysed. The linear perturbation analysis serves as the basis for the study of the role of wave motions in inertia-free polarity transitions in nonlinear dynamo models, given in §3. Here, we find that the formation of the axial dipole from a chaotic multipolar state and the collapse of the axial dipole into a polarity-reversing state are dynamically similar phenomena, in that they both occur at $|\omega_A/\omega_M| \sim 1$. While dipole formation requires the excitation of slow

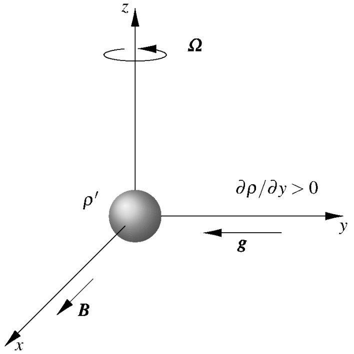

Figure 1: The initial state of a density perturbation ρ' that evolves in an unstably stratified rotating fluid subject to a uniform magnetic field.

MAC waves as a dynamo evolves from a small seed magnetic field, polarity reversals occur when the slow waves are suppressed in a strongly driven dynamo. The self-similarity of the dipole–multipole transition in the inertia-free regime places a constraint on the Rayleigh number for reversals. In §4, we discuss the implications of our results for planetary cores and future work.

2. Evolution of a density disturbance under rapid rotation and a magnetic field

2.1. *Problem set-up and governing equations*

A localized density disturbance ρ' that occurs in an unstably stratified rotating fluid layer threaded by a uniform magnetic field is considered. Since ρ' is related to a temperature perturbation Θ by $\rho' = -\rho\alpha\Theta$, where ρ is the ambient density and α is the coefficient of thermal expansion, an initial temperature perturbation is chosen in the form

$$\Theta_0 = C\exp\left[-(x^2+y^2+z^2)/\delta^2\right], \tag{2.1}$$

where C is a constant and δ is the length scale of the perturbation. Figure 1 shows the initial perturbation which subsequently evolves under gravity $\boldsymbol{g} = -g\hat{\boldsymbol{e}}_y$, background rotation $\boldsymbol{\Omega} = \Omega\hat{\boldsymbol{e}}_z$ and a uniform magnetic field $\boldsymbol{B} = B\hat{\boldsymbol{e}}_x$ in Cartesian coordinates (x, y, z). In an otherwise quiescent medium, the initial temperature perturbation (2.1) gives rise to a velocity field $\boldsymbol{u}$, which in turn interacts with $\boldsymbol{B}$ to generate the induced magnetic field $\boldsymbol{b}$. The initial velocity $\boldsymbol{u}_0$ and induced field $\boldsymbol{b}_0$ are both zero. In the Boussinesq approximation, the following magnetohydrodynamic (MHD) equations give the evolution of $\boldsymbol{u}$, $\boldsymbol{b}$ and Θ:

$$\frac{\partial \boldsymbol{u}}{\partial t} = -\frac{1}{\rho}\nabla p^* - 2\boldsymbol{\Omega}\times\boldsymbol{u} + \frac{1}{\mu\rho}(\boldsymbol{B}\cdot\nabla)\boldsymbol{b} - \boldsymbol{g}\alpha\Theta + \nu\nabla^2\boldsymbol{u}, \tag{2.2}$$

$$\frac{\partial \boldsymbol{b}}{\partial t} = (\boldsymbol{B}\cdot\nabla)\boldsymbol{u} + \eta\nabla^2\boldsymbol{b}, \tag{2.3}$$

$$\frac{\partial \Theta}{\partial t} = -\gamma\hat{\boldsymbol{e}}_y\cdot\boldsymbol{u} + \kappa\nabla^2\Theta, \tag{2.4}$$

$$\nabla\cdot\boldsymbol{u} = \nabla\cdot\boldsymbol{b} = 0, \tag{2.5}$$

where ν is the kinematic viscosity, κ is the thermal diffusivity, η is the magnetic diffusivity, μ is the magnetic permeability, $\boldsymbol{\Omega} = \Omega \hat{\boldsymbol{e}}_z$, $p^* = p - (\rho/2)|\boldsymbol{\Omega} \times \boldsymbol{x}|^2 + \boldsymbol{b}^2/2\mu$ and $\gamma = \partial T_0/\partial y < 0$ is the mean temperature gradient in the unstably stratified fluid.

2.2. *Solutions for the velocity field*

Taking the curl of equations (2.2) and the (2.3) and eliminating the electric current density between them, we obtain for the velocity field,

$$\begin{aligned}
&\left[\left(\frac{\partial}{\partial t} - \nu\nabla^2\right)\left(\frac{\partial}{\partial t} - \eta\nabla^2\right) - V_M^2 \frac{\partial^2}{\partial x^2}\right]^2 (-\nabla^2 \boldsymbol{u}) \\
&\quad = 4\Omega^2 \left(\frac{\partial}{\partial t} - \eta\nabla^2\right)^2 \frac{\partial^2 \boldsymbol{u}}{\partial z^2} - 2\Omega\alpha \frac{\partial}{\partial z}\left(\frac{\partial}{\partial t} - \eta\nabla^2\right)^2 (\nabla \times \Theta \boldsymbol{g}) \\
&\quad - \alpha \left(\frac{\partial}{\partial t} - \eta\nabla^2\right)\left[\left(\frac{\partial}{\partial t} - \nu\nabla^2\right)\left(\frac{\partial}{\partial t} - \eta\nabla^2\right) - V_M^2 \frac{\partial^2}{\partial x^2}\right](\nabla \times \nabla \times \Theta \boldsymbol{g}),
\end{aligned} \tag{2.6}$$

where $V_M = B/\sqrt{\mu\rho}$ is the Alfvén velocity. The assumption of an unbounded domain facilitates the use of Fourier transforms along each coordinate direction,

$$\mathscr{F}(\mathbf{A}) = \hat{\mathbf{A}} = \frac{1}{(2\pi)^3} \int_{-\infty}^{\infty}\int_{-\infty}^{\infty}\int_{-\infty}^{\infty} \mathbf{A} \mathrm{e}^{-\mathrm{i}\boldsymbol{k}\cdot\boldsymbol{x}}\, \mathrm{d}x\, \mathrm{d}y\, \mathrm{d}z, \tag{2.7}$$

and

$$\mathscr{F}^{-1}\left(\hat{\mathbf{A}}\right) = \mathbf{A} = \int_{-\infty}^{\infty}\int_{-\infty}^{\infty}\int_{-\infty}^{\infty} \hat{\mathbf{A}} \mathrm{e}^{\mathrm{i}\boldsymbol{k}\cdot\boldsymbol{x}}\, \mathrm{d}k_x\, \mathrm{d}k_y\, \mathrm{d}k_z, \tag{2.8}$$

where $\boldsymbol{k} = (k_x, k_y, k_z)$ represents the wave vector such that $|\boldsymbol{k}| = k = \sqrt{k_x^2 + k_y^2 + k_z^2}$. Application of the Fourier transform (2.7) to the Cartesian components of equation (2.6) gives

$$\begin{aligned}
&\left[\left(\left(\frac{\partial}{\partial t} + \omega_\nu\right)\left(\frac{\partial}{\partial t} + \omega_\eta\right) + \omega_M^2\right)^2 \left(\frac{\partial}{\partial t} + \omega_\kappa\right) + \omega_C^2 \left(\frac{\partial}{\partial t} + \omega_\eta\right)^2 \left(\frac{\partial}{\partial t} + \omega_\kappa\right)\right] \hat{u}_x \\
&\quad = \left[-\omega_C \omega_A^2 \frac{k_z k}{k_x^2 + k_z^2}\left(\frac{\partial}{\partial t} + \omega_\eta\right)^2\right. \\
&\quad \left. + \omega_A^2 \frac{k_x k_y}{k_x^2 + k_z^2}\left(\frac{\partial}{\partial t} + \omega_\eta\right)\left(\left(\frac{\partial}{\partial t} + \omega_\nu\right)\left(\frac{\partial}{\partial t} + \omega_\eta\right) + \omega_M^2\right)\right] \hat{u}_y,
\end{aligned} \tag{2.9}$$

$$\begin{aligned}
&\left[\left(\left(\frac{\partial}{\partial t} + \omega_\nu\right)\left(\frac{\partial}{\partial t} + \omega_\eta\right) + \omega_M^2\right)^2 \left(\frac{\partial}{\partial t} + \omega_\kappa\right) + \omega_C^2 \left(\frac{\partial}{\partial t} + \omega_\eta\right)^2 \left(\frac{\partial}{\partial t} + \omega_\kappa\right)\right. \\
&\quad \left. + \omega_A^2 \left(\frac{\partial}{\partial t} + \omega_\eta\right)\left(\left(\frac{\partial}{\partial t} + \omega_\nu\right)\left(\frac{\partial}{\partial t} + \omega_\eta\right) + \omega_M^2\right)\right] \hat{u}_y = 0,
\end{aligned} \tag{2.10}$$

$$\begin{aligned}
&\left[\left(\left(\frac{\partial}{\partial t} + \omega_\nu\right)\left(\frac{\partial}{\partial t} + \omega_\eta\right) + \omega_M^2\right)^2 \left(\frac{\partial}{\partial t} + \omega_\kappa\right) + \omega_C^2 \left(\frac{\partial}{\partial t} + \omega_\eta\right)^2 \left(\frac{\partial}{\partial t} + \omega_\kappa\right)\right] \hat{u}_z \\
&\quad = \left[\omega_C \omega_A^2 \frac{k_x k}{k_x^2 + k_z^2}\left(\frac{\partial}{\partial t} + \omega_\eta\right)^2\right. \\
&\quad \left. + \omega_A^2 \frac{k_y k_z}{k_z^2 + k_x^2}\left(\frac{\partial}{\partial t} + \omega_\eta\right)\left(\left(\frac{\partial}{\partial t} + \omega_\nu\right)\left(\frac{\partial}{\partial t} + \omega_\eta\right) + \omega_M^2\right)\right] \hat{u}_y,
\end{aligned} \tag{2.11}$$

where we have combined the transformed temperature equation (2.4) with the transform of (2.6). In equations (2.9)–(2.11),

$$\omega_C^2 = 4\Omega^2 k_z^2/k^2, \quad \omega_A^2 = g\alpha\gamma\left(k_x^2 + k_z^2\right)/k^2, \quad \omega_M^2 = V_M^2 k_x^2, \tag{2.12}$$

represent the squares of the frequencies of linear inertial, buoyancy and Alfvén waves respectively (Braginsky 1967; Busse *et al.* 2007). In an unstably stratified medium, wherein $\omega_A^2 < 0$, $|\omega_A|$ is a measure of the strength of buoyancy. As the present study focuses on a system where the viscous and thermal diffusion are much smaller than magnetic diffusion, the frequencies $\omega_\nu = \nu k^2$ and $\omega_\kappa = \kappa k^2$ in (2.9)–(2.11) are small compared $\omega_\eta = \eta k^2$. In this limit, the solution of the form $\hat{u}_y \sim \mathrm{e}^{\mathrm{i}\lambda t}$ for the homogeneous equation (2.10) gives the following quintic equation in λ:

$$\begin{aligned} \lambda^5 - 2\mathrm{i}\omega_\eta\lambda^4 - (\omega_A^2 + \omega_C^2 + \omega_\eta^2 + 2\omega_M^2)\lambda^3 + 2\mathrm{i}\omega_\eta(\omega_A^2 + \omega_C^2 + \omega_M^2)\lambda^2 \\ + (\omega_A^2\omega_\eta^2 + \omega_C^2\omega_\eta^2 + \omega_A^2\omega_M^2 + \omega_M^4)\lambda - \mathrm{i}\omega_A^2\omega_\eta\omega_M^2 = 0, \end{aligned} \tag{2.13}$$

the approximate roots of which were discussed in Sreenivasan & Maurya (2021) for known relative orders of magnitudes of ω_M, ω_A, ω_C and ω_η. In the solution for (2.10),

$$\hat{u}_y = \sum_{m=1}^{5} D_m \mathrm{e}^{\mathrm{i}\lambda_m t}, \tag{2.14}$$

the coefficients D_m are determined using the initial conditions for $\hat{u}_y$ and its time derivatives (§2.3). Of the five terms in the expansion on the right-hand side of (2.14), two terms represent oppositely travelling fast MAC waves, two other terms represent oppositely travelling slow MAC waves, and the fifth term represents the overall growth of the velocity perturbation.

By substituting (2.14) in (2.9) and (2.11), the following solutions for (2.9) and (2.11) are obtained:

$$\hat{u}_x = \hat{u}_x^H + \hat{u}_x^P = \sum_{m=1}^{5} A_m \mathrm{e}^{\mathrm{i}\lambda_m^H t} + \sum_{m=1}^{5} M_m e^{\mathrm{i}\lambda_m^P t}, \tag{2.15}$$

$$\hat{u}_z = \hat{u}_z^H + \hat{u}_z^P = \sum_{m=1}^{5} C_m \mathrm{e}^{\mathrm{i}\lambda_m^H t} + \sum_{m=1}^{5} N_m e^{\mathrm{i}\lambda_m^P t} \tag{2.16}$$

In (2.15) and (2.16), $\hat{u}_x^H$ and $\hat{u}_z^H$ are the homogeneous solutions of (2.9) and (2.11) respectively, $\hat{u}_x^P$ and $\hat{u}_z^P$ are the particular solutions, λ_m^P are the roots of (2.13) and λ_m^H are the roots of (2.13) with $\omega_A = 0$,

$$\begin{aligned} \lambda_1^H &= \frac{1}{2}\left(\omega_C + \mathrm{i}\omega_\eta + \sqrt{\omega_C^2 - 2\mathrm{i}\omega_C\omega_\eta - \omega_\eta^2 + 4\omega_M^2}\right), \\ \lambda_2^H &= \frac{1}{2}\left(-\omega_C + \mathrm{i}\omega_\eta - \sqrt{\omega_C^2 + 2\mathrm{i}\omega_C\omega_\eta - \omega_\eta^2 + 4\omega_M^2}\right), \\ \lambda_3^H &= \frac{1}{2}\left(\omega_C + \mathrm{i}\omega_\eta - \sqrt{\omega_C^2 - 2\mathrm{i}\omega_C\omega_\eta - \omega_\eta^2 + 4\omega_M^2}\right), \\ \lambda_4^H &= \frac{1}{2}\left(-\omega_C + \mathrm{i}\omega_\eta + \sqrt{\omega_C^2 + 2\mathrm{i}\omega_C\omega_\eta - \omega_\eta^2 + 4\omega_M^2}\right), \\ \lambda_5^H &= 0, \end{aligned} \tag{2.17}$$

which give the frequencies of the fast and slow Magneto-Coriolis (MC) waves in the absence of buoyancy (Sreenivasan & Narasimhan 2017). The coefficients A_m, C_m, M_m and N_m in (2.15) and (2.16) are evaluated as in §2.3 below.

The solutions for the induced magnetic field transforms $\hat{b}_x$, $\hat{b}_y$ and $\hat{b}_z$ are obtained following a similar approach.

2.3. *Evaluation of spectral coefficients*

From (2.14), the initial conditions for $\hat{u}_y$ and its time derivatives are given by

$$\mathrm{i}^n \sum_{m=1}^{5} D_m \lambda_m^n = \left(\frac{\partial^n \hat{u}_y}{\partial t^n}\right)_{t=0} = a_{n+1},\ n=0,1,2,3,4. \tag{2.18}$$

Algebraic simplifications give the right-hand sides of (2.18) in the limit of $\nu = \kappa = 0$, as follows:

$$\begin{aligned}
a_1 &= \hat{u}_y|_{t=0} = 0,\\
a_2 &= \frac{\partial \hat{u}_y}{\partial t}|_{t=0} = \alpha g \left(\frac{k_z^2 + k_x^2}{k^2}\right) \hat{\Theta}_0,\\
a_3 &= \frac{\partial^2 \hat{u}_y}{\partial t^2}|_{t=0} = 0,\\
a_4 &= \frac{\partial^3 \hat{u}_y}{\partial t^3}|_{t=0} = -(\omega_M^2 + \omega_C^2 + \omega_A^2)\, a_2,\\
a_5 &= \frac{\partial^4 \hat{u}_y}{\partial t^4}|_{t=0} = \omega_M^2 \omega_\eta\, a_2.
\end{aligned} \tag{2.19}$$

The coefficients D_m may now be obtained using the roots of equation (2.13). For example, we obtain,

$$D_1 = \frac{a_5 - \mathrm{i}a_4(\lambda_2 + \lambda_3 + \lambda_4 + \lambda_5) + \mathrm{i}a_2(\lambda_2\lambda_4\lambda_5 + \lambda_3\lambda_4\lambda_5 + \lambda_2\lambda_3\lambda_4 + \lambda_2\lambda_3\lambda_5)}{(\lambda_1 - \lambda_2)(\lambda_1 - \lambda_3)(\lambda_1 - \lambda_4)(\lambda_1 - \lambda_5)}, \tag{2.20}$$

$$D_3 = \frac{a_5 - \mathrm{i}a_4(\lambda_1 + \lambda_2 + \lambda_4 + \lambda_5) + \mathrm{i}a_2(\lambda_1\lambda_4\lambda_5 + \lambda_2\lambda_4\lambda_5 + \lambda_1\lambda_2\lambda_4 + \lambda_1\lambda_2\lambda_5)}{(\lambda_3 - \lambda_1)(\lambda_3 - \lambda_2)(\lambda_3 - \lambda_4)(\lambda_3 - \lambda_5)}, \tag{2.21}$$

for the forward-travelling fast and slow wave solutions respectively. The coefficients A_m and C_m are determined in a similar way. The coefficients M_m and N_m in equations (2.15) and (2.16) are obtained using the method of undetermined coefficients, as follows:

$$\begin{aligned}
M_m = \frac{D_m}{T_m}\Bigg[&- \omega_C \omega_A^2 \left(\frac{k k_z}{k_x^2 + k_z^2}\right) \left(-(\lambda_m^P)^2 + \omega_\eta^2 + 2\mathrm{i}\omega_\eta \lambda_m^P\right)\\
&+ \omega_A^2 \frac{k_x k_y}{k_x^2 + k_z^2} \left(-\mathrm{i}(\lambda_m^P)^3 - 2\omega_\eta (\lambda_m^P)^2 + \mathrm{i}(\omega_\eta^2 + \omega_M^2)\lambda_m^P + \omega_M^2 \omega_\eta\right)\Bigg],
\end{aligned} \tag{2.22}$$

and

$$\begin{aligned}
N_m = \frac{D_m}{T_m}\Bigg[&\omega_C \omega_A^2 \left(\frac{k k_x}{k_x^2 + k_z^2}\right) \left(-(\lambda_m^P)^2 + \omega_\eta^2 + 2\mathrm{i}\omega_\eta \lambda_m^P\right)\\
&+ \omega_A^2 \frac{k_z k_y}{k_x^2 + k_z^2} \left(-\mathrm{i}(\lambda^P)^3 - 2\omega_\eta (\lambda_m^P)^2 + \mathrm{i}(\omega_\eta^2 + \omega_M^2)\lambda_m^P + \omega_M^2 \omega_\eta\right)\Bigg],
\end{aligned} \tag{2.23}$$

with

$$\begin{aligned}
T_m = \mathrm{i}(\lambda_m^P)^5 + 2(\lambda_m^P)^4 \omega_\eta - \mathrm{i}(\lambda_m^P)^3(\omega_C^2 + \omega_\eta^2 + 2\omega_M^2) - 2\omega_\eta (\lambda_m^P)^2 (2\omega_C^2 + \omega_M^2)\\
+ \mathrm{i}\lambda_m^P(\omega_C^2 \omega_\eta^2 + \omega_M^4), \quad m = 1, 2 \ldots 5.
\end{aligned} \tag{2.24}$$

2.4. *Fast and slow MAC waves in unstable stratification*

The solution of the initial value problem gives the velocity and induced magnetic fields at discrete points in time. The analysis of the solutions is limited to times much shorter than the time scale for the exponential increase of the perturbations. When the buoyancy force is small compared with the Lorentz force ($|\omega_A/\omega_M| \ll 1$), the parameter regime is determined by the

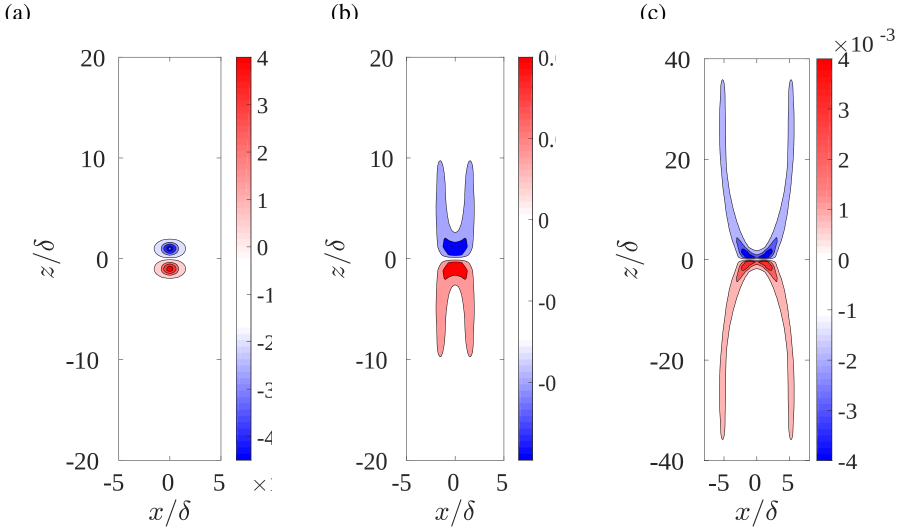

Figure 2: Evolution of the kinetic helicity on the *x*-*z* plane at $y = 0$ with time (measured in units of the magnetic diffusion time t_η) for $Le = 0.03$ and $E_\eta = 2 \times 10^{-5}$. The snapshots are at (a) $t/t_\eta = 1 \times 10^{-4}$, (b) $t/t_\eta = 2.5 \times 10^{-3}$ and (c) $t/t_\eta = 1 \times 10^{-2}$. The ratio $|\omega_A/\omega_M| = 0.05$ at times after the formation of the waves.

Lehnert number Le and the magnetic Ekman number E_η,

$$Le = \frac{V_M}{2\Omega\delta}, \quad E_\eta = \frac{\eta}{2\Omega\delta^2}, \tag{2.25a,b}$$

both based on the length scale δ of the initial buoyancy perturbation (2.1).

Figure 2 shows the evolution of the kinetic helicity $\boldsymbol{u} \cdot \boldsymbol{\zeta}$ at $y = 0$. The real-space fields are obtained from the transforms $\hat{\boldsymbol{u}}$ and $\hat{\boldsymbol{\zeta}}$ via the inverse Fourier transform (2.8). Here, a truncation value of $\pm 10/\delta$ is used for the three wavenumbers in the integrals since the initial wavenumber $k_0 = \sqrt{3}/\delta$. Apart from the spatial segregation of oppositely signed helicity between the two halves about the mid-plane $z = 0$ (e.g. Ranjan *et al.* 2020), the evolution of blobs into columnar structures through the propagation of damped waves is evident.

As an important aim of this study is to understand the role of MAC waves in the dipolar and multipolar dynamo regimes, we may separate the fast and slow MAC wave parts of the general solution, which is a linear superposition of the two wave solutions. For example,

$$\begin{aligned}
\hat{u}_{x,f} &= M_1 e^{i\lambda_1^P t} + M_2 e^{i\lambda_2^P t} + A_1 e^{i\lambda_1^H t} + A_2 e^{i\lambda_2^H t}, \\
\hat{u}_{y,f} &= D_1 e^{i\lambda_1 t} + D_2 e^{i\lambda_2 t}, \\
\hat{u}_{z,f} &= N_1 e^{i\lambda_1^P t} + N_2 e^{i\lambda_2^P t} + C_1 e^{i\lambda_1^H t} + C_2 e^{i\lambda_2^H t},
\end{aligned} \tag{2.26}$$

and

$$\begin{aligned}
\hat{u}_{x,s} &= M_3 e^{i\lambda_3^P t} + M_4 e^{i\lambda_4^P t} + A_3 e^{i\lambda_3^H t} + A_4 e^{i\lambda_4^H t}, \\
\hat{u}_{y,s} &= D_3 e^{i\lambda_3 t} + D_4 e^{i\lambda_4 t}, \\
\hat{u}_{z,s} &= N_3 e^{i\lambda_3^P t} + N_4 e^{i\lambda_4^P t} + C_3 e^{i\lambda_3^H t} + C_4 e^{i\lambda_4^H t},
\end{aligned} \tag{2.27}$$

where the subscripts f and s in the left-hand sides of (2.26) and (2.27) denote the fast and slow wave parts of the solution.

Figure 3(a) shows the variation of fundamental frequencies with Le. The range of $|\omega_M/\omega_C|$

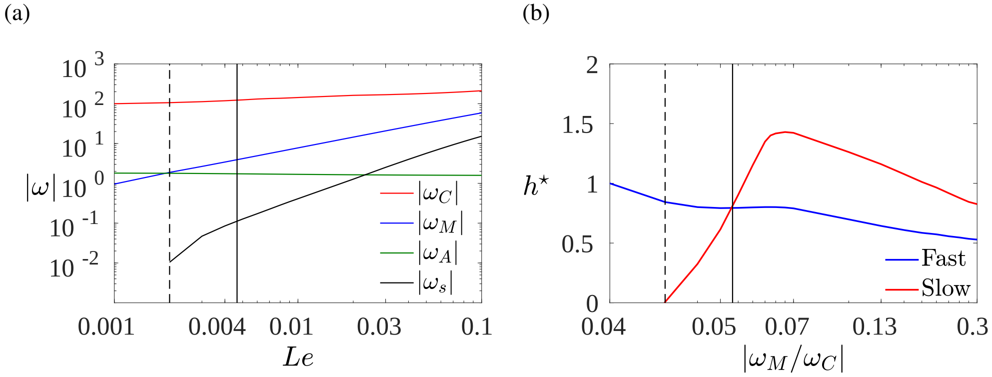

Figure 3: (a) Variation of absolute values of frequencies with *Le*. (b) Variation of the total kinetic helicity in the region $z < 0$ with $|\omega_M/\omega_C|$. The range of $|\omega_M/\omega_C|$ in (b) corresponds to the range of *Le* in (a). All calculations are performed for $E_\eta = 2 \times 10^{-5}$. The slow wave frequency, ω_s takes non-zero values for $Le > 2 \times 10^{-3}$, when $|\omega_M| > |\omega_A|$.

on the horizontal axis of figure 3(b) corresponds to the range of *Le* in figure 3(a). The values of $|\omega_M/\omega_C|$ are systematically higher than that of *Le*, which is essentially the initial value of this ratio. The enhanced instantaneous value of $|\omega_M/\omega_C|$ is due to the anisotropy of the columnar flow (see Varma & Sreenivasan 2022), and would not be evident if $\boldsymbol{\Omega}$ were aligned with $\boldsymbol{B}$ (Sreenivasan & Maurya 2021). For $E_\eta = 2 \times 10^{-5}$, all calculations for $Le > 2 \times 10^{-3}$ satisfy the inequality $|\omega_C| > |\omega_M| > |\omega_A| > |\omega_\eta|$, thought to be essential for axial dipole formation in convective dynamos. Figure 3(b) shows the variation of the dimensionless helicity h^* of the fast and slow MAC waves, obtained by summing the helicity at all points in (x, z) for $z < 0$ and $y = 0$ and then normalizing this value by the nonmagnetic helicity. For $Le > 2 \times 10^{-3}$ ($|\omega_M/\omega_C| > 0.045$), the slow wave helicity increases dramatically, and for $Le \sim 10^{-2}$ ($|\omega_M/\omega_C| \sim 0.1$), the slow wave helicity is greater than the fast wave helicity. This result is consistent the dominance of the slow waves over the fast waves for $|\omega_M/\omega_C| \sim 0.1$ in the energy-containing scales in numerical dynamo models (Varma & Sreenivasan 2022).

In figure 4, the contours of the fast and slow MAC wave helicities are shown at two times for $|\omega_M/\omega_C| = 0.13$, which lies in the region of slow wave dominance in figure 3(b). The fast waves split in two and propagate rapidly along z. The slow waves do not propagate as far as the fast waves at the same time due to their lower group velocity. Yet, as indicated by the colour bars, the slow waves are markedly more intense than the fast waves. Both fast and slow wave columns propagate along x at the Alfvén velocity (see figure 5 below).

The effect of progressively increasing the buoyant forcing on the fast and slow waves is examined in the following section. It is anticipated that strong forcing would selectively attenuate the slow waves, with implications for polarity transitions in dynamos.

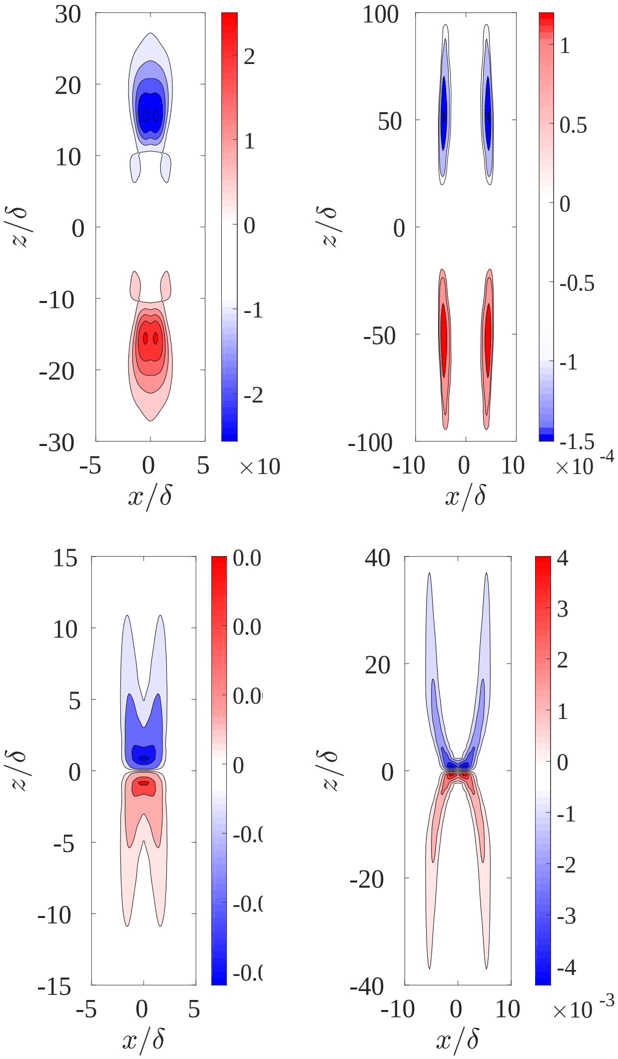

Figure 4: Helicity on the section $y = 0$ of fast (a, b) and slow (c,d) MAC waves at two times, $t/t_\eta = 2.5 \times 10^{-3}$ (left panels) and $t/t_\eta = 1 \times 10^{-2}$ (right panels). Here, $E_\eta = 2 \times 10^{-5}$ and $Le = 0.03$ ($|\omega_M/\omega_C| = 0.13$).

2.5. *Effect of progressively increasing buoyancy*

For the regime given by $|\omega_C| \gg |\omega_M| \gg |\omega_A| \gg |\omega_\eta|$, the roots of the homogeneous equation (2.13) are approximated by (Sreenivasan & Maurya 2021)

$$\lambda_{1,2} \approx \pm \left(\omega_C + \frac{\omega_M^2}{\omega_C} \right) + \mathrm{i}\, \frac{\omega_M^2 \omega_\eta}{\omega_C^2}, \tag{2.28}$$

$$\lambda_{3,4} \approx \pm \left(\frac{\omega_M^2}{\omega_C} + \frac{\omega_A^2}{2\omega_C} \right) + \mathrm{i}\, \omega_\eta \left(1 - \frac{\omega_A^2}{2\omega_M^2} \right), \tag{2.29}$$

$$\lambda_5 \approx \mathrm{i}\, \frac{\omega_A^2 \omega_\eta}{\omega_M^2}. \tag{2.30}$$

As $|\omega_A|$ increases relative to $|\omega_M|$, the fast MAC waves, given by frequencies $\lambda_{1,2}$, are unaffected except by weak magnetic diffusion. However, the slow waves, whose real frequencies are approximated by

$$\mathrm{Re}(\lambda_{3,4}) \approx \pm\left(\frac{\omega_M^2}{\omega_C} + \frac{\omega_A^2}{2\omega_C}\right) \approx \pm\frac{\omega_M^2}{\omega_C}\left(1+\frac{\omega_A^2}{\omega_M^2}\right)^{1/2} \tag{2.31}$$

for $\omega_C| \gg |\omega_M|, |\omega_A|$ (Braginsky 1967), would be significantly attenuated in an unstably stratified fluid as $|\omega_A|$ nears $|\omega_M|$. We see below that the decrease of the slow wave frequency translates into the marked decrease of the slow wave helicity relative to the fast wave helicity.

Figure 5(a) indicates that both fast and slow MAC waves propagate along the mean-field direction x such that $x/\delta = t/t_a$, where t_a is the Alfvén wave travel time. For small $|\omega_A/\omega_M|$, the helicity of slow wave motions is greater than that of fast waves, but as $|\omega_A/\omega_M|$ approaches unity, the slow wave helicity weakens considerably and falls below that of the fast wave. The effect of increasing buoyancy forcing on the fast and slow wave helicity is shown graphically in figure 6. The fast waves are practically unaffected by the strength of forcing as their intensity and z propagation rate are nearly invariant for $|\omega_A/\omega_M|$ in the range 0.1–1 (figure 6(a–c)). The slow wave helicity, on the other hand, is substantially attenuated as $|\omega_A/\omega_M|$ increases in the same range (figure 6(d–f)). For $|\omega_A/\omega_M| \approx 1$, a state is reached where the slow wave helicity is nearly zero. The induced magnetic field b_z also weakens considerably with increasing $|\omega_A/\omega_M|$ (figure 6(g–i)), which indicates that only the slow wave helicity has a direct bearing on field generation.

Figure 5(b) shows the normalized slow wave helicity against a ‘local’ Rayleigh number based on the length scale of the initial perturbation,

$$Ra_\ell = \frac{g\alpha|\gamma|\delta^2}{2\Omega\eta} \tag{2.32}$$

as well as $|\omega_A/\omega_M|$. Evidently, the forcing needed to suppress the slow waves increases with Le, although the total suppression of these waves occurs universally at $|\omega_A/\omega_M| \approx 1$. This result prompts us to look at the condition for vanishing slow wave helicity through a relation between Ra_ℓ and a parameter Λ defined by

$$\Lambda = \left(\frac{\omega_M^2}{\omega_C\omega_\eta}\right)_0 \sim \frac{V_M^2}{2\Omega\eta}, \tag{2.33}$$

which measures the initial ratio of the slow MC wave frequency to the magnetic diffusion frequency. Figure 7 shows that the same linear relation between Ra_ℓ and Λ, whose values are tabulated in table 1, holds for any E_η. Both Ra_ℓ and Λ are measurable in dynamo models, the latter being of the same order of magnitude as the Elsasser number – the square of the scaled magnetic field – in many models. In low-inertia dynamos where the nonlinear inertial force is small compared with the Coriolis force, we may expect self-similarity of Ra_ℓ with respect to Λ, as suggested by figure 7. If the state of vanishing slow wave helicity is taken as a proxy for polarity transitions, then the value of Ra_ℓ in this state can provide a useful constraint on the Rayleigh number that admits magnetic reversals. This idea is explored further in §3.

3. Nonlinear dynamo simulations

We consider a convection-driven dynamo operating in a spherical shell, the boundaries of which correspond to the inner core boundary (ICB) and the core–mantle boundary (CMB). The ratio of inner to outer radius is 0.35. Fluid motion is driven by thermal buoyancy, although our formulation can also study thermochemical buoyancy using the codensity formulation (Braginsky & Roberts 1995). The other body forces acting on the fluid are the electromagnetic Lorentz

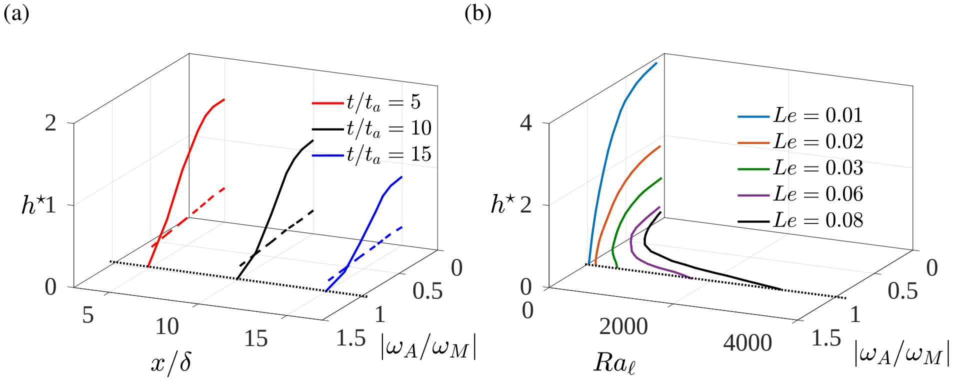

Figure 5: (a) Variation of the fast wave (dashed line) and slow wave (solid line) helicity for $z < 0$, normalized by the non-magnetic helicity, with x/δ and $|\omega_A/\omega_M|$ at different times (measured in units of the Alfvén wave travel time t_a). Here, $E_\eta = 2 \times 10^{-5}$ and $Le = 0.03$. (b) Variation of the normalized slow wave helicity with the local Rayleigh number Ra_ℓ (defined in (2.32)) and $|\omega_A/\omega_M|$ for different Le.

$E_\eta = 6 \times 10^{-7}$			$E_\eta = 6 \times 10^{-6}$			$E_\eta = 2 \times 10^{-5}$		
Le	Λ	Ra_ℓ $\times 10^4$	Le	Λ	Ra_ℓ $\times 10^4$	Le	Λ	Ra_ℓ $\times 10^4$
0.0071	47	0.0380	0.0120	13.67	0.0097	0.0200	11.87	0.0039
0.0111	118	0.1227	0.0366	127.49	0.1383	0.0601	107.33	0.1258
0.0139	185	0.2029	0.0509	246.04	0.2669	0.0901	240.68	0.2538
0.0162	253	0.2832	0.0620	365.39	0.3956	0.1063	335.34	0.3787
0.0201	338	0.4437	0.0704	470.60	0.5242	0.1201	428.41	0.5036
0.0233	523	0.6042	0.0779	575.81	0.6528	0.1344	536.45	0.6286
0.0262	658	0.7647	0.0846	680.00	0.7814	0.1472	653.35	0.7535
0.0287	793	0.9252	0.0908	782.69	0.9100	0.1589	749.42	0.8784
0.0311	928	1.0862	0.0966	885.38	1.0386	0.1698	858.50	1.0035
0.0322	996	1.1335	0.1020	988.07	1.1672	0.1800	961.57	1.1283

Table 1: Values of Ra_ℓ, defined in (2.32), at different Λ, defined in (2.33), for suppression of slow MAC waves in the linear magnetoconvection calculations. The dimensionless parameters Le and E_η are defined in (2.25a,b).

force and the Coriolis force. Lengths are scaled by the thickness of the spherical shell L and time is scaled by magnetic diffusion time L^2/η, where η is magnetic diffusivity. The velocity $\boldsymbol{u}$ and magnetic field $\boldsymbol{B}$ are scaled by η/L and $(2\Omega\rho\mu\eta)^{1/2}$, respectively, where Ω is the rotation rate, ρ is the fluid density and μ is the magnetic permeability. The temperature is scaled by βL, where β is the radial temperature gradient at the outer boundary. In the Boussinesq approximation, the non-dimensional MHD equations for the velocity, magnetic field and temperature are given by,

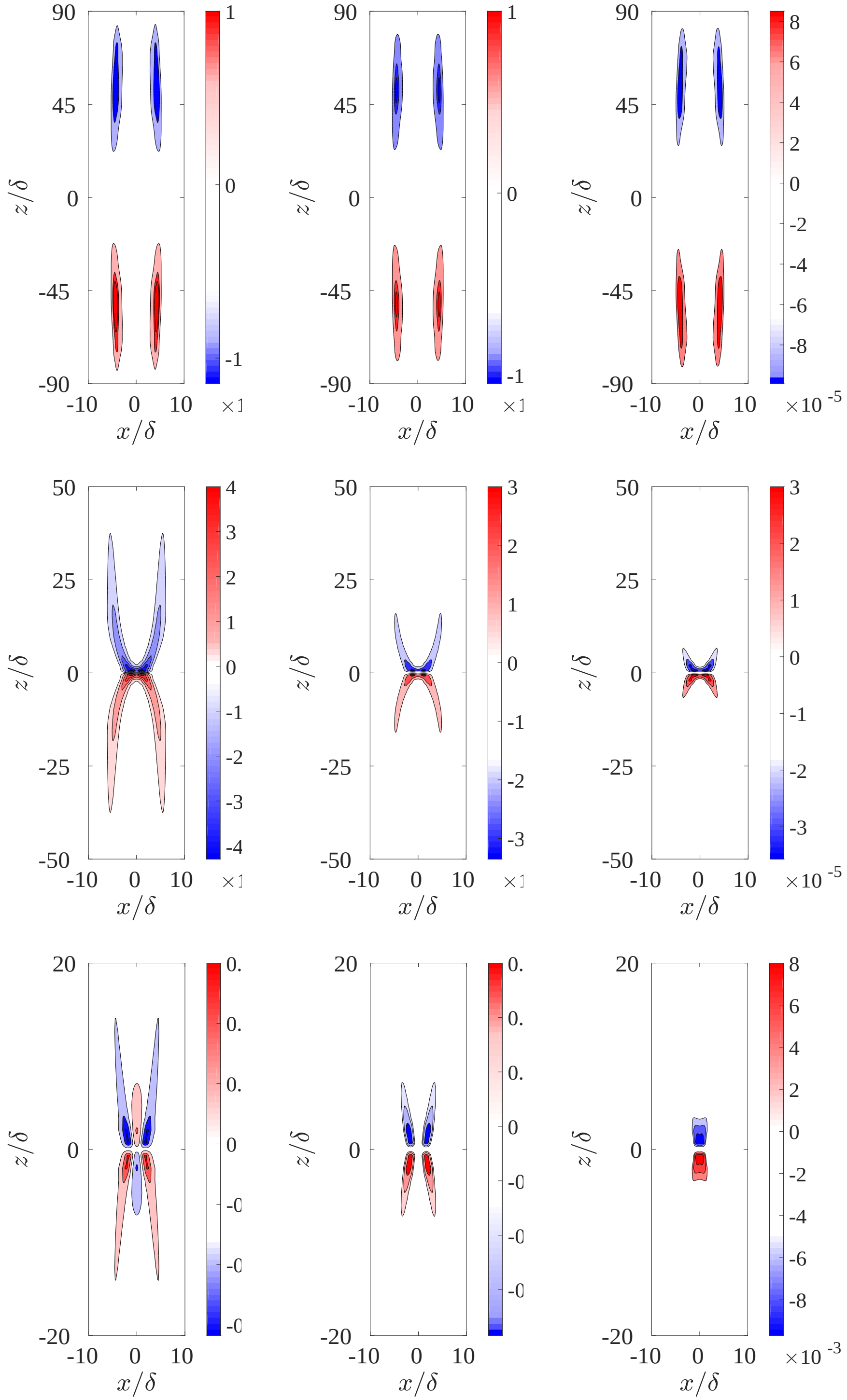

Figure 6: Fast MAC wave helicity (a–c), slow MAC wave helicity (d–f) and z-component of the induced magnetic field, b_z (g–i) for $|\omega_A/\omega_M| = 0.1$, 0.6, 0.95 (left to right). The plots are generated at time $t/t_\eta = 0.01$ for the parameters $Le = 0.03$ and $E_\eta = 2\times10^{-5}$.

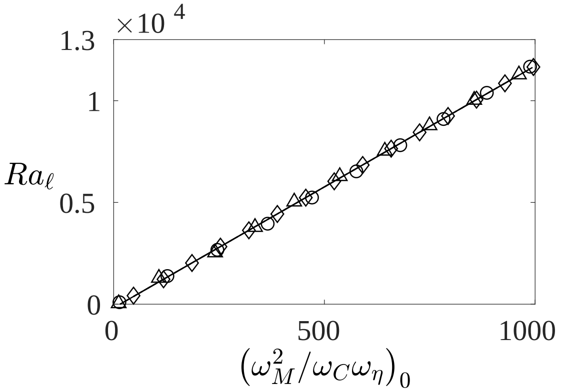

Figure 7: Variation of the local Rayleigh number Ra_ℓ, defined in (2.32), shown against Λ, defined in (2.33), for the state of approximately zero slow MAC wave helicity. Three values of E_η are considered – the diamonds represent $E_\eta = 6\times10^{-7}$, circles represent $E_\eta = 6\times10^{-6}$ and triangles represent $E_\eta = 2\times10^{-5}$.

$$EPm^{-1}\left(\frac{\partial \boldsymbol{u}}{\partial t} + (\nabla\times\boldsymbol{u})\times\boldsymbol{u}\right) + \hat{\boldsymbol{z}}\times\boldsymbol{u} = -\nabla p^\star + Ra\,Pm Pr^{-1}\,T\,\boldsymbol{r} + (\nabla\times\boldsymbol{B})\times\boldsymbol{B} + E\nabla^2\boldsymbol{u}, \tag{3.1}$$

$$\frac{\partial \boldsymbol{B}}{\partial t} = \nabla\times(\boldsymbol{u}\times\boldsymbol{B}) + \nabla^2\boldsymbol{B}, \tag{3.2}$$

$$\frac{\partial T}{\partial t} + (\boldsymbol{u}\cdot\nabla)T = PmPr^{-1}\,\nabla^2 T, \tag{3.3}$$

$$\nabla\cdot\boldsymbol{u} = \nabla\cdot\boldsymbol{B} = 0, \tag{3.4}$$

The modified pressure p^* in equation (3.1) is given by $p + E\,Pm^{-1}\,|\boldsymbol{u}|^2$. The dimensionless parameters in the above equations are the Ekman number $E = \nu/2\Omega L^2$, the Prandtl number, $Pr = \nu/\kappa$, the magnetic Prandtl number, $Pm = \nu/\eta$ and the modified Rayleigh number $g\alpha\beta L^2/2\Omega\kappa$. Here, g is the gravitational acceleration, ν is the kinematic viscosity, κ is the thermal diffusivity and α is the coefficient of thermal expansion.

The basic-state temperature profile represents a basal heating given by $T_0(r) = r_i r_o/r$, where r_i and r_o are the inner and outer radii of the spherical shell. The velocity and magnetic fields satisfy the no-slip and electrically insulating conditions respectively at the two boundaries. The inner boundary is isothermal while the outer boundary has constant heat flux. The calculations are performed by a pseudospectral code that uses spherical harmonic expansions in the angular coordinates (θ,ϕ) and finite differences in radius r (Willis *et al.* 2007).

As in earlier studies (Sreenivasan & Jones 2011; Varma & Sreenivasan 2022), the dynamo simulations begin from a dipole-dominated seed magnetic field of volume-averaged intensity $\bar{B} = 0.01$. The main output parameters of the dynamo simulations, given in table 2, are time-averaged values in the saturated state of the dynamo. For three values of the Ekman number E, a series of simulations at progressively increasing Rayleigh number Ra are performed, spanning the dipole-dominated regime up to the onset of polarity reversals. The mean spherical harmonic degrees for convection and energy injection are defined by

$$l_c = \frac{\Sigma\, l\, E_k(l)}{\Sigma\, E_k(l)};\;\; l_E = \frac{\Sigma\, l\, E_T(l)}{\Sigma\, E_T(l)}, \tag{3.5}$$

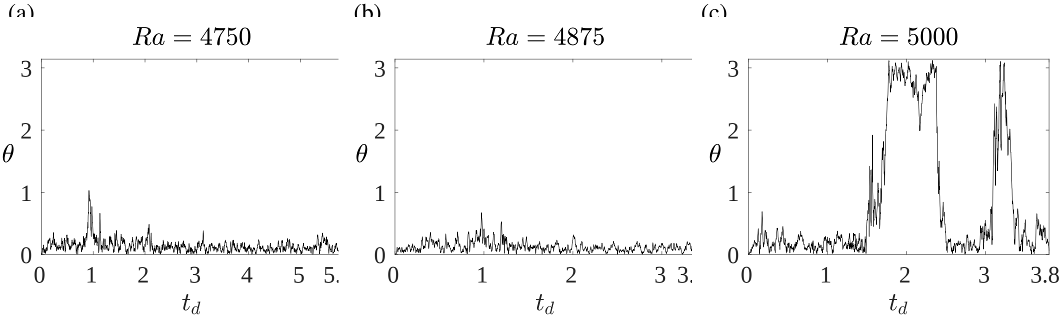

Figure 8: Dipole colatitude versus magnetic diffusion time at (a) $Ra = 4750$, (b) $Ra = 4875$ and (c) $Ra = 5000$. The other parameters are $E = 3\times10^{-4}, Pm = Pr = 20$.

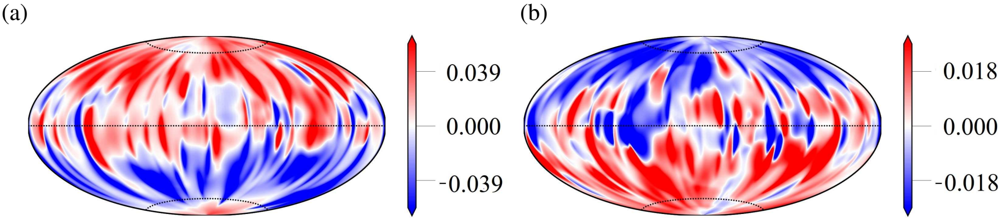

Figure 9: The contours of the radial magnetic field for $Ra = 5000$ at the outer boundary for magnetic diffusion times (a) $t_d = 1.24$ and (b) $t_d = 1.9$ The other dynamo parameters are $E = 3\times10^{-4}, Pm = Pr = 20$.

where $E_k(l)$ is the kinetic energy spectrum and $E_T(l)$ is the spectrum obtained from the product of the transform of u_rT and its conjugate. For each E, the value of $Pm = Pr$ is chosen such that the local Rossby number Ro_ℓ, which gives the ratio of the inertial to Coriolis forces on the characteristic length scale of convection (Christensen & Aubert 2006) is < 0.1 (table 2). Therefore, our dynamo simulations lie in the rotationally dominant, or low-inertia, regime.

Figure 8 shows the magnetic colatitude of the dipole field, θ at the upper boundary obtained from spherical harmonic coefficients, as follows:

$$\cos\theta = g_1^0/|\boldsymbol{m}|, \quad \boldsymbol{m} = (g_1^0, g_1^1, h_1^1), \tag{3.6}$$

and

$$g_1^0 = \mathscr{P}_1^0,\ g_1^1 = -2\,\mathrm{Re}(\mathscr{P}_1^1),\ h_1^1 = 2\,\mathrm{Im}(\mathscr{P}_1^1), \tag{3.7}$$

where $\mathscr{P}$ is the poloidal part of the magnetic field. For $E = 3\times10^{-4}$ and $Pr = Pm =$20, the dipole axis flips by 180° at $Ra = 5000$ (figure 8(c)), as confirmed by the contour plots of the radial magnetic field in figure 9 (a) & (b).

As in earlier studies (Varma & Sreenivasan 2022), the range of spherical harmonic degrees $l \leqslant l_E$ is of particular interest since kinetic helicity is known to be generated in the nonlinear dynamo in this range of energy-containing scales. A relative helicity is defined that measures the augmentation of lower-hemisphere helicity in the nonlinear dynamo (magnetic) run relative to that in the equivalent nonmagnetic simulation.

$$H_r = \frac{h_m - h_{nm}}{h_{nm}}, \tag{3.8}$$

for $l \leqslant l_E$. Here, the subscripts m and nm denote the magnetic (dynamo) and nonmagnetic values respectively. The variation of H_r with time in dynamos that evolve from a small seed field is

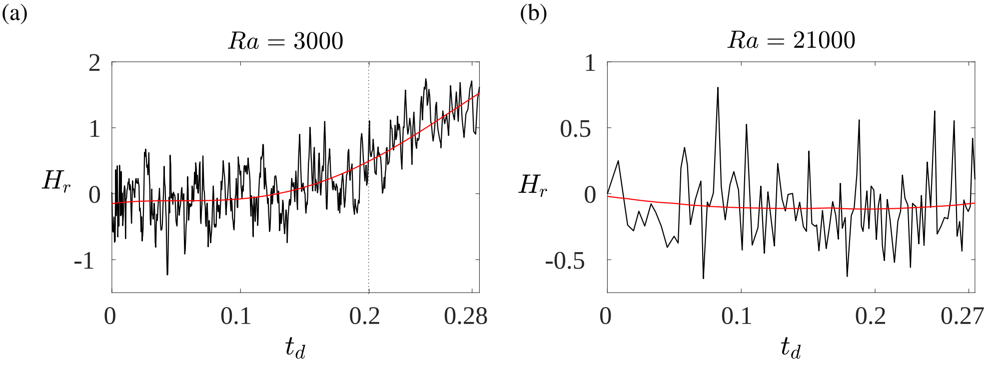

Figure 10: Relative helicity, H_r, as defined in (3.8), in two dynamo simulations starting from a seed magnetic field. The evolution of H_r is shown for two runs, (a) $Ra = 3000$ (dipole-dominated) and (b) $Ra = 21000$ (polarity-reversing). The superposed red line is a polynomial fit showing the trend of the evolution. The dotted vertical line in (a) marks the formation of stable dipole field in the run. The other dynamo parameters are $E = 6 \times 10^{-5}$, $Pm = Pr = 5$.

given in figure 10. While there is an approximately two-fold increase in helicity for the dipole-dominated run, there is no noticeable increase in helicity in the polarity-reversing run over the nonmagnetic state. This result prompts us to examine the nature of wave motions in the dipolar and reversing runs.

3.1. *Attenuation of slow MAC waves in polarity-reversing dynamos*

Isolated density disturbances in a rotating stratified fluid layer excite MAC waves whose frequencies depend on the fundamental frequencies ω_M, ω_A and ω_C, representing Alfvén waves, internal gravity waves and linear inertial waves respectively. In unstable stratification that drives planetary core convection, $\omega_A^2 < 0$, where $|\omega_A|$ is simply a measure of the strength of buoyancy. Since the dimensional frequencies ω_M^2, $-\omega_A^2$ and ω_C^2 in the dynamo are given by (Varma & Sreenivasan 2022)

$$\omega_M^2 = \frac{(\boldsymbol{B}\cdot\boldsymbol{k})^2}{\mu\rho}, \quad -\omega_A^2 = g\alpha\beta\left(\frac{k_z^2+k_\phi^2}{k^2}\right), \quad \omega_C^2 = \frac{4(\boldsymbol{\Omega}\cdot\boldsymbol{k})^2}{k^2}, \tag{3.9}$$

and scaling the frequencies by η/L^2, we obtain in dimensionless units,

$$\omega_M^2 = \frac{Pm}{E}(\boldsymbol{B}\cdot\boldsymbol{k})^2, \quad -\omega_A^2 = \frac{Pm^2 Ra}{Pr\,E}\left(\frac{{k_z}^2+k_\phi^2}{k^2}\right), \quad \omega_C^2 = \frac{Pm^2}{E^2}\frac{k_z^2}{k^2}, \tag{3.10}$$

where k_s, k_ϕ and k_z are the radial, azimuthal and axial wavenumbers in cylindrical coordinates (s,ϕ,z), $k_\phi = m/s$, where m is the spherical harmonic order, and $k^2 = k_s^2 + k_\phi^2 + k_z^2$. Here, ω_A is evaluated on the equatorial plane where the buoyancy force is maximum. The magnetic (Alfvén) wave frequency ω_M is based on the three components of the measured magnetic field at the peak-field location. The wavenumber k_ϕ is evaluated at $s = 1$, approximately mid-radius of the spherical shell.

For the inequality $|\omega_C| > |\omega_M| > |\omega_A|$, the fast (f) and slow (s) MAC waves are given by the following frequencies in the diffusionless limit (Busse *et al.* 2007; Salhi *et al.* 2017):

$$\omega_f = \pm\frac{1}{\sqrt{2}}\sqrt{\omega_A^2+\omega_C^2+2\omega_M^2+\sqrt{\omega_A^4+2\omega_A^2\omega_C^2+4\omega_M^2\omega_C^2+\omega_C^4}}, \tag{3.11}$$

$$\omega_s = \pm\frac{1}{\sqrt{2}}\sqrt{\omega_A^2+\omega_C^2+2\omega_M^2-\sqrt{\omega_A^4+2\omega_A^2\omega_C^2+4\omega_M^2\omega_C^2+\omega_C^4}}. \tag{3.12}$$

While the fast waves are linear inertial waves weakly modified by the magnetic field and buoyancy, the slow waves are magnetostrophic.

In figure 11, the magnitudes of the fundamental frequencies are shown as a function of the spherical harmonic order m in the saturated state of the dynamo run at $E = 6\times10^{-5}$, and $Pr = Pm = 5$. The frequencies are computed from (3.10) using the mean values of the s and z wavenumbers. For example, real space integration over (s,ϕ) gives the kinetic energy as a function of z, the Fourier transform of which gives the one-dimensional spectrum $\hat{u}^2(k_z)$. Subsequently, we obtain

$$\bar{k}_z = \frac{\Sigma k_z\,\hat{u}^2(k_z)}{\Sigma \hat{u}^2(k_z)}. \tag{3.13}$$

A similar approach gives $\bar{k}_s$. The computed frequencies in figure 11(a)–(c), shown for dynamos with $Ra = 6000$–18000, satisfy the inequality $|\omega_C| > |\omega_M| > |\omega_A|$ in a range of the spherical harmonic order m. The dashed vertical lines show the value of m below which the helicity in the nonlinear dynamo is greater than that in the nonmagnetic run at the same parameters. Evidently, the scales of helicity generation in the nonlinear dynamo overlaps with the scales where the slow MAC waves are generated. The range of m over which the above frequency inequality holds narrows down with Ra, and for the polarity-reversing dynamo with $Ra = 21000$, this inequality does not exist at any m (figure 11(d)).

The spectral distribution of the power supplied to the poloidal part of the axial dipole field B_{10}^P, given by (e.g. Buffett & Bloxham 2002)

$$P_{10} = \int_V \boldsymbol{B}_{10}^P\cdot[\nabla\times(\boldsymbol{u}\times\boldsymbol{B})_m]\,dV, \tag{3.14}$$

also given in figure 11 (a)–(d), suggests that the axial dipole is predominantly generated in the scales where the MAC waves are generated. In the reversing dynamo without the MAC wave window, the power supplied to the dipole is small.

In figure 12, the dynamo frequencies are computed from (3.10) using the mean values of the s, ϕ and z wavenumbers in the saturated state of the dynamo in the range $l \leqslant l_E$, which represents the energy-containing scales. The mean spherical harmonic order $\bar{m}$ is evaluated through a weighted average as in (3.13), but over the range of m within $l \leqslant l_E$. As the field increases from a small seed value in the dipolar dynamo run at $Ra = 3000$ (figure 12(a)), slow MAC waves of frequency ω_s are thought to be first excited when $|\omega_M| > |\omega_A|$ (see Varma & Sreenivasan 2022). The formation of the axial dipole from a chaotic field, marked by the dotted vertical line, follows slow wave excitation. In the run at $Ra = 21000$ where polarity reversals occur, $|\omega_M|$ remains lower than $|\omega_A|$ throughout (figure 12(b)), so the slow waves are never excited. From the variation of the frequencies with increasing strength of forcing, given in figure 12(c), we note that $|\omega_M|$ falls below $|\omega_A|$ at $Ra \approx 21000$, which indicates that polarity reversals would indeed onset in the regime $|\omega_M| \approx |\omega_A|$ when slow MAC waves disappear. The volume-averaged mean square value of the axial dipole field is much smaller in the reversing regime of $Ra = 21000$ than in the stable dipole regime of $Ra = 3000$ (figure 12(d)), which suggests that the slow MAC waves have an important role in the formation of the axial dipole.

Figure 13 shows the measurement of wave motion in the saturated state of dynamos at $E = 6\times10^{-5}$ and $Pr = Pm = 5$ and three values of Ra spanning the dipole-dominated regime and

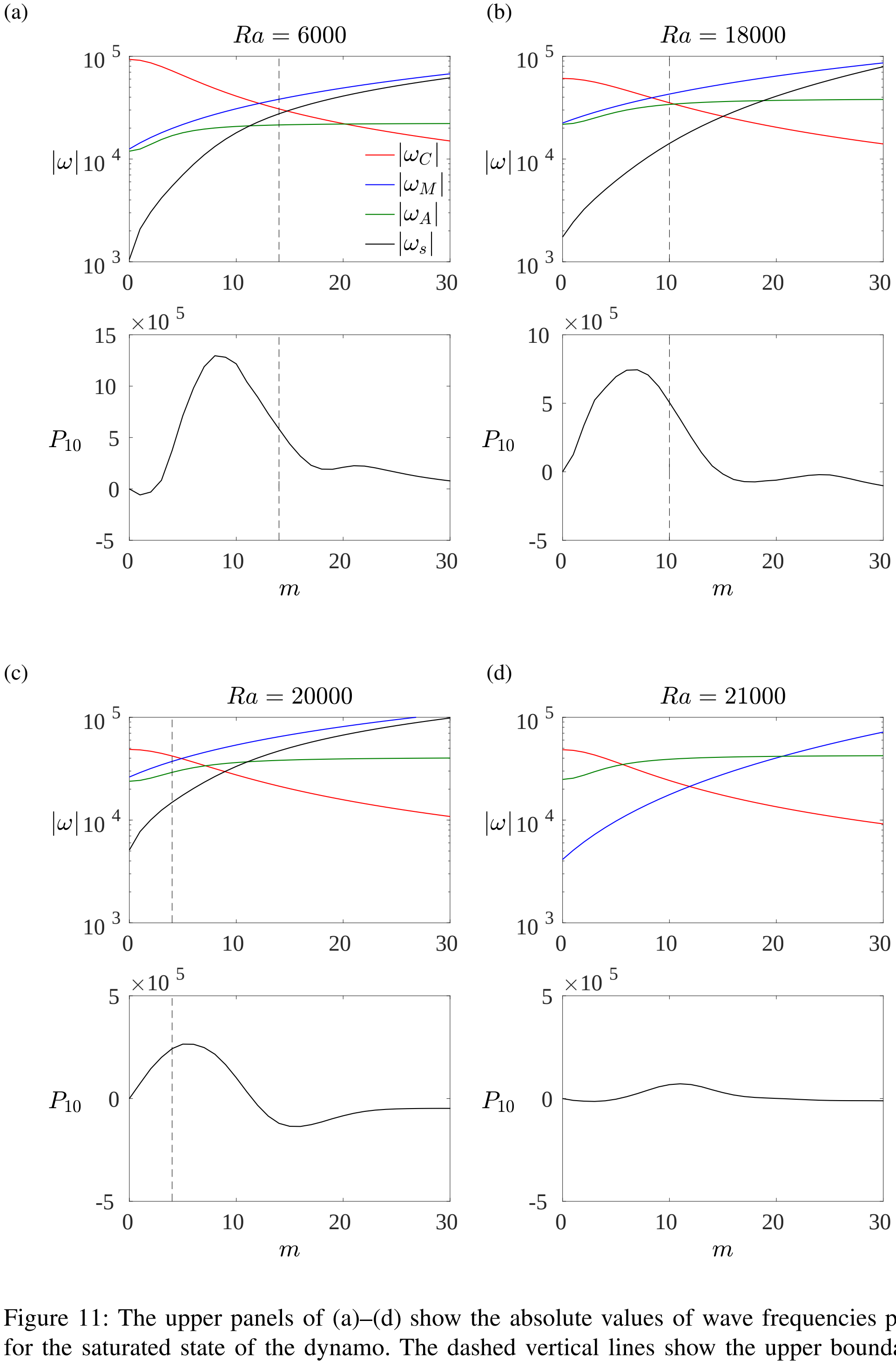

Figure 11: The upper panels of (a)–(d) show the absolute values of wave frequencies plotted for the saturated state of the dynamo. The dashed vertical lines show the upper boundary of the range of wavenumbers m for which the the helicity of the dynamo run is greater than that of the equivalent nonmagnetic run. The lower panels of (a)–(d) show the spectral distribution of the power supplied to the axial dipole, defined in (3.14). The modified Rayleigh number Ra of the model is given above each panel. The other dynamo parameters are $E = 6 \times 10^{-5}$, and $Pr = Pm = 5$.

Ra	Ra/Ra_c	N_r	l_{max}	Rm	Ro_ℓ	l_E	l_C	$\bar{m}$	$\bar{k}_s$	$\bar{k}_z$	B^2_{rms}	Ra_ℓ	Λ
$E = 3\times 10^{-4}, Pm = Pr = 20$													
400	18.2	72	64	56	0.002	11	8	3.52	2.92	2.87	0.59	1274	24
800	36.4	72	64	75	0.003	11	9	3.91	3.65	2.81	1.11	2066	48
1600	72.7	72	72	106	0.005	13	10	4.12	3.32	2.43	1.12	3721	64
2000	90.9	72	72	119	0.005	14	11	4.34	3.01	2.97	0.98	4192	87
2400	109.1	72	96	130	0.006	14	11	4.26	3.14	2.66	0.87	5221	114
3000	136.4	72	96	148	0.007	15	11	4.31	3.52	2.24	0.58	6376	128
4000	181.8	72	96	171	0.009	15	11	4.19	3.25	2.63	0.49	8995	160
4500	204.6	132	128	192	0.009	15	11	4.34	2.87	2.54	0.47	9432	167
4750	215.9	132	128	199	0.010	15	11	4.29	3.43	2.46	0.46	10189	179
4875	221.6	132	132	203	0.010	15	11	4.16	3.26	2.19	0.46	11121	185
4950	225.0	132	132	105	0.011	15	11	4.12	3.11	2.42	0.32	11513	195
5000	227.3	132	132	210	0.011	15	11	4.02	3.35	2.31	0.003	12215	$210^\star$
$E = 6\times 10^{-5}, Pm = Pr = 5$													
300	10.3	88	96	67	0.002	10	9	3.89	3.81	3.36	0.52	783	26
400	13.8	88	96	74	0.002	11	9	3.78	4.21	3.25	0.74	1105	29
1000	34.5	128	120	98	0.004	16	12	4.69	3.86	3.31	2.48	1795	39
3000	103.5	160	160	169	0.009	20	15	5.23	4.75	4.29	3.26	4330	96
6000	206.9	160	160	243	0.014	22	16	5.92	5.51	4.13	3.28	6759	126
8000	275.9	160	180	288	0.020	23	17	6.14	5.27	3.62	3.29	8377	149
12000	413.8	160	180	365	0.024	24	17	7.13	4.68	3.34	3.27	9319	160
14000	482.8	160	180	402	0.026	25	18	7.54	5.11	2.97	3.18	9722	185
18000	620.7	160	180	456	0.032	25	19	7.78	4.84	3.30	3.04	11740	200
20000	689.7	160	180	505	0.035	25	19	8.12	4.64	3.46	2.55	11975	215
21000	724.1	160	180	549	0.039	25	19	8.05	4.22	3.38	0.62	12793	$227^\star$
$E = 1.2\times 10^{-5}, Pm = Pr = 1$													
300	10.3	90	96	78	0.004	15	15	4.87	3.87	2.86	0.31	499	17
700	24.1	90	96	102	0.005	19	17	5.02	4.25	3.02	2.11	1097	18
1000	34.5	132	144	112	0.006	21	20	5.12	4.58	2.89	2.46	1506	36
2500	86.2	168	160	174	0.011	26	20	6.54	4.04	2.82	3.59	2308	38
4000	137.9	180	168	224	0.017	28	20	7.94	4.14	3.42	4.01	2505	41
10000	344.8	192	180	384	0.033	33	24	9.13	4.62	3.07	5.04	4736	67
15000	517.2	192	180	500	0.045	34	24	9.87	4.87	2.97	5.35	6079	95
20000	689.7	192	180	573	0.052	35	25	9.93	4.43	3.12	5.46	8007	139
25000	862.1	192	180	655	0.061	36	25	10.01	4.48	2.78	5.84	9850	176
27000	931.0	192	180	698	0.065	36	25	9.96	4.69	2.87	4.87	10745	190
28000	965.5	192	180	775	0.073	36	25	10.05	4.81	2.91	0.82	10944	$196^\star$

Table 2: Summary of the main input and output parameters in the dynamo simulations considered in this study. Here, Ra is the modified Rayleigh number, Ra_c is the modified critical Rayleigh number for onset of nonmagnetic convection, N_r is the number of radial grid points, l_{max} is the maximum spherical harmonic degree, Rm is the magnetic Reynolds number, Ro_ℓ is the local Rossby number, l_C and l_E are the mean spherical harmonic degrees of convection and energy injection respectively (defined in (3.5)), $\bar{m}$ is the mean spherical harmonic order in the range $l \leqslant l_E$, $\bar{k}_s$ and $\bar{k}_z$ are the mean s and z wavenumbers in the range $l \leqslant l_E$, Ra_ℓ is the local Rayleigh number defined in (3.15), B^2_{rms} is the measured mean square value of the field in the saturated dynamo and Λ is the peak Elsasser number obtained from the square of the measured peak field at the earliest time of excitation of slow MAC waves in the dynamo run starting from a small seed field. *The last run in each Ekman number series is a polarity-reversing dynamo, for which Λ is the square of the measured peak field when slow MAC waves cease to exist in the run starting from the saturated state of the penultimate run in that series (also see §3.2).

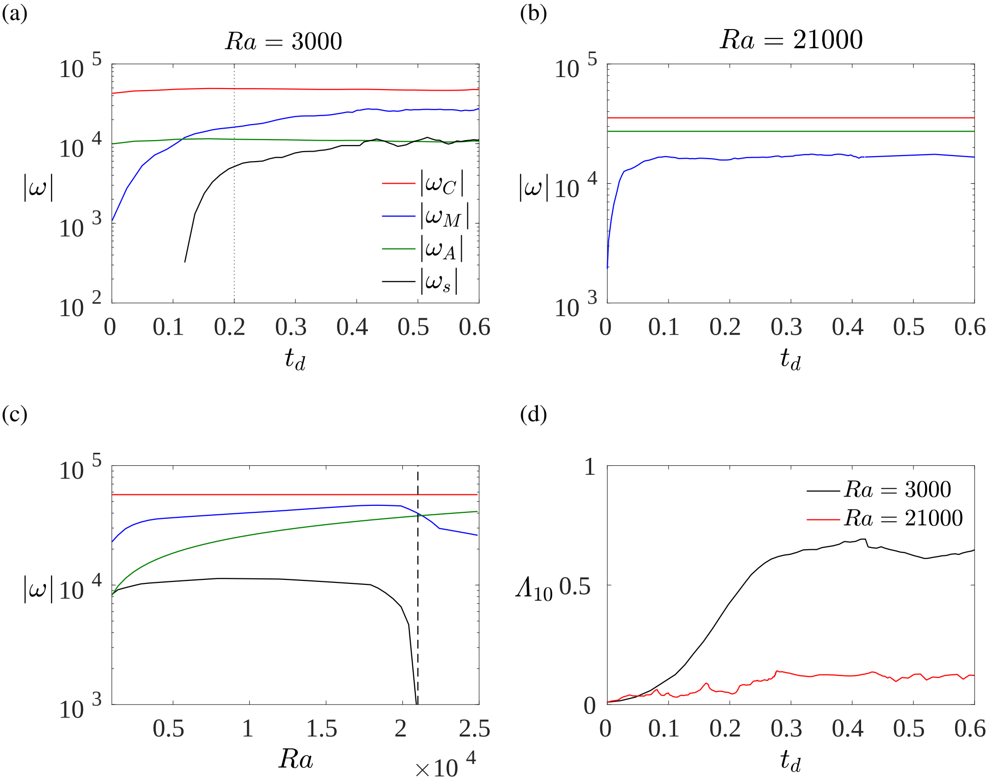

Figure 12: (a) & (b) Absolute values of the measured frequencies ω_M, ω_A, ω_C and ω_s plotted against time (measured in units of the magnetic diffusion time, t_d). The simulations study the evolution of the dynamo starting from a small seed magnetic field. The modified Rayleigh number Ra is shown above each panel. The dotted vertical line in (a) marks the time of formation of the axial dipole from a multipolar field. (c) Frequencies in the saturated dynamo shown against Ra. The dashed vertical line here gives the value of Ra at which the slow MAC wave frequency ω_s goes to zero. (d) The Elsasser number of the axial dipole field component, based on its root mean square value, for $Ra = 3000$ and $Ra = 21000$. The dynamo parameters are $E = 6\times10^{-5}$, $Pm = Pr = 5$. The colour codes in (a) are also used in (b) and (c).

reversals. Contours of $\dot{u}_z$ at cylindrical radius $s = 1$ are plotted over small time windows in which the ambient magnetic field and wavenumbers are approximately constant. These contours show the propagation paths of the fluctuating z velocity. In line with the discussion so far and Varma & Sreenivasan (2022), the measurement of axial motions is limited to the energy-containing scales $l \leqslant l_E$, with no restriction on the wavenumber. The measured axial group velocity of the waves, $U_{g,z}$ – obtained from the slope of the black lines in figure 13 – is compared with the estimated fast (U_f) and slow (U_s) group velocities obtained by taking the derivatives of the respective frequencies in (3.11) and (3.12) with respect to k_z (table 3). The theoretical frequencies ω_f and ω_s are estimated using the three components of the magnetic field at the peak-field location and the mean values of k_s, k_z and m over the range of energy-containing scales, $l \leqslant l_E$. In the dipole-dominated run at $Ra = 6000$, both fast and slow MAC waves co-exist, although the slow waves are dominant (shown in two different ϕ locations in figure 13(a) and (b)). At $Ra = 20000$, the increasing occurrence of the fast waves at the same location as the slow waves is noted by the nearly vertical propagation paths (figure 13(c)). The measured slow wave group velocity at

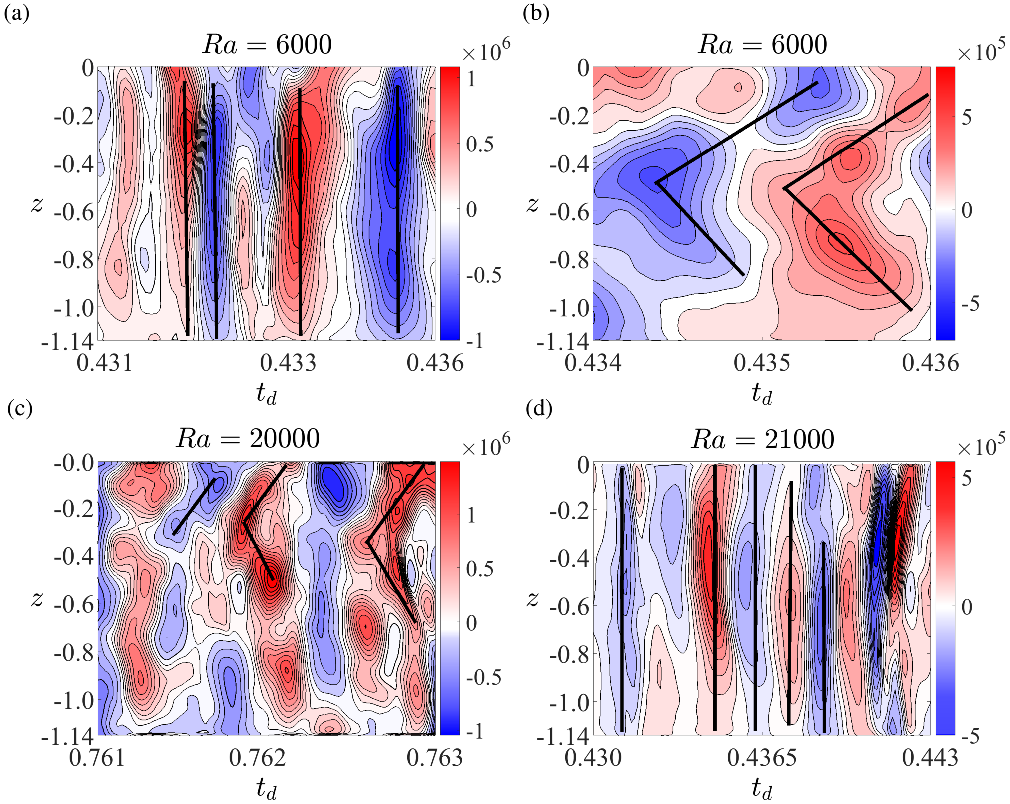

Figure 13: Contour plots of $\partial u_z/\partial t$ at cylindrical radius $s = 1$ for $l \leqslant l_E$ and small intervals of time in the saturated state of three dynamo simulations. The parallel black lines indicate the predominant direction of travel of the waves and their slope gives the group velocity. The Rayleigh number Ra of the simulation is given above each panel. The other dynamo parameters are $E = 6 \times 10^{-5}$, $Pr = Pm = 5$. The estimated group velocity of the fast and slow MAC waves (U_f and U_s respectively) and the measured group velocity $U_{g,z}$ are given in table 3.

$Ra = 20000$ is greater than that at $Ra = 6000$, which reflects the larger self-generated field at the higher Rayleigh number. In the reversing dynamo at $Ra = 21000$, slow waves are totally absent while the fast waves are abundant (figure 13(d)).

The dominance of the slow MAC waves in the dipole-dominated dynamo and the fast MAC waves in the reversing dynamo is further evident in figure 14, where the fast Fourier transform (FFT) of $\dot{u}_z$ is shown. The flow largely consists of waves of frequency $\omega \sim \omega_s$ in the dipolar dynamo (figure 14(a)), whereas in the reversing dynamo, waves of much higher frequency $\omega \sim \omega_f$ are dominant (figure 14(b)).

3.2. *Self-similarity of the dipole–multipole transition*

In the presence of small but finite magnetic diffusion, the slow MAC waves are known to disappear in an unstably stratified medium for $|\omega_A/\omega_M| \approx 1$. The same condition must hold for the appearance of slow waves in a medium where the magnetic field progressively increases from a small value. In simulations starting from a small seed field, the earliest time of excitation of the slow MAC waves is noted from group velocity measurements at closely spaced times during the growth phase of the dynamo. The peak Elsasser number $\Lambda = B^2$ at this time is obtained from

	E	Ra	Fig. No.	ω_n^2 $(\times 10^{10})$	ω_C^2 $(\times 10^8)$	ω_M^2 $(\times 10^8)$	$-\omega_A^2$ $(\times 10^8)$	ω_f $(\times 10^4)$	ω_s $(\times 10^4)$	U_f	U_s	$U_{g,z}$
1	6×10^{-5}	6000	13(a)	1.6	22.27	5.98	3.67	5.48	0.67	7454	368	7072
2	6×10^{-5}	6000	13(b)	1.6	22.27	5.98	3.67	5.48	0.67	7454	368	391
3	6×10^{-5}	20000	–	1.44	18.94	17.72	13.45	6.24	1.39	7029	2124	9784
4	6×10^{-5}	20000	13(c)	1.44	18.94	17.72	13.45	6.24	1.39	7029	2124	1146
5	6×10^{-5}	21000	13(d)	0.53	17.84	13.93	14.05	5.63	0	7214	–	10587

Table 3: Summary of the data for MAC wave measurement in the dynamo models. The sampling frequency ω_n is chosen to ensure that the fast MAC waves are not missed in the measurement of group velocity. The values of ω_M^2, $-\omega_A^2$ and ω_C^2 are calculated from (3.10) using the mean values of m, k_s and k_z over the range of energy-containing scales, $l \leqslant l_E$. The measured group velocity in the z direction ($U_{g,z}$) is compared with the estimated fast (U_f) or slow (U_s) MAC wave velocity.

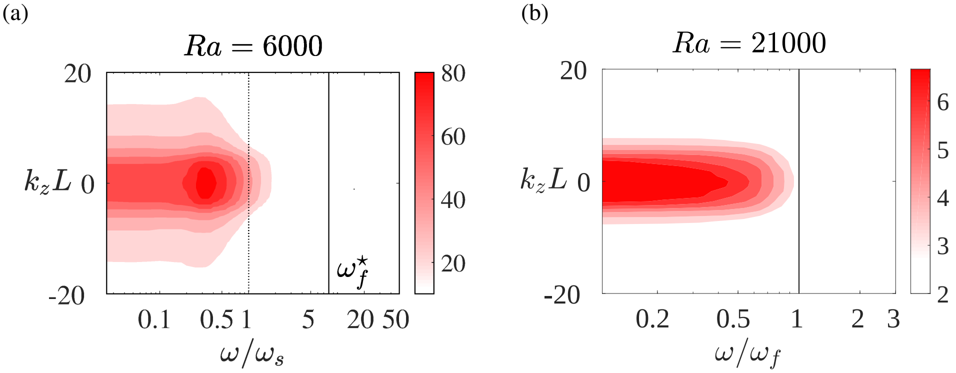

Figure 14: (c) FFT spectrum of $\partial u_z/\partial t$ at cylindrical radius $s = 1$ for the scales $l \leqslant l_E$. The spectra are computed at discrete ϕ points and then averaged azimuthally. The dotted vertical line in (a) corresponds to $\omega/\omega_s = 1$ and the solid vertical line in (b) corresponds to $\omega/\omega_f = 1$, where ω_f and ω_s are the estimated fast and slow MAC wave frequencies. In (a), $\omega_f^\star = \omega_f/\omega_s$. The Rayleigh number in the simulation is given above each panel. The other dynamo parameters are $E = 6\times10^{-5}$ and $Pm = Pr = 5$.

the three components of the field at the peak-field location, and presented in the last column of table 2. In each of the three dynamo series considered in this study, the last run is a polarity-reversing dynamo, for which Λ is the measured peak Elsasser number when slow MAC waves cease to exist in the run starting from the saturated state of the penultimate run in that series. Figure 15(a) shows that the variation of Ra with Λ in the three dynamo series is nearly linear. The Rayleigh number corresponding to reversals (at which slow MAC waves disappear) lies on this line, indicating that the appearance and disappearance of MAC waves are in dynamically similar regimes.

Following the analysis in figure 7, where the Rayleigh number based on the length scale of the buoyant perturbation was studied, we define a local Rayleigh number in the dynamo,

$$Ra_\ell = \frac{g\alpha\beta}{2\Omega\eta}\left(\frac{2\pi}{\bar{m}}\right)^2, \tag{3.15}$$

where $\bar{m}$ is the mean spherical harmonic order evaluated over m within the energy-containing

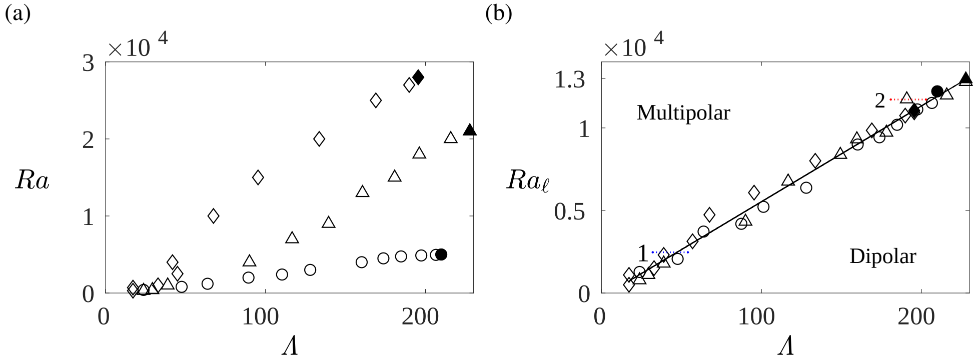

Figure 15: (a) Variation of the modified Rayleigh number Ra with the peak Elsasser number Λ (square of the peak magnetic field) at both excitation and suppression of slow MAC waves. The hollow symbols represent the states where slow waves are first excited as the dynamos evolve from a small seed field; the filled symbols represent the states where slow waves are suppressed in the polarity-reversing dynamos. The parameters of the three dynamo series and their symbolic representations are as follows: $E = 3 \times 10^{-4}, Pm = Pr = 20$ (circles), $E = 6 \times 10^{-5}, Pm = Pr = 5$ (triangles), $E = 1.2 \times 10^{-5}, Pm = Pr = 1$ (diamonds). (b) Variation of the local Rayleigh number Ra_ℓ, defined in (3.15), with Λ. The values of Ra, Ra_ℓ and Λ in the plots are given in table 2. The sections 1 and 2 marked on the self-similar line are analysed further in figures 16 and 17 below.

scales $l \leqslant l_E$. The behaviour of Ra_ℓ, which is defined for the scales where the MAC waves are excited by buoyancy, is self-similar (figure 15(b)). The values of Ra_ℓ at the onset of polarity reversals, where the slow MAC waves disappear, also lie on the same self-similar branch. While the conventional Rayleigh numbers Ra at the onset of reversals in the three dynamo series lie far apart (see the filled symbols in figure 15(a)), the respective local Rayleigh numbers Ra_ℓ are remarkably close, and $\sim 10^4$ (see the filled symbols in figure 15(b) and table 2). The magnetic Ekman number based on $\bar{m}$ in the three dynamo series takes values of $E_\eta \sim 10^{-5}$ for a wide range of Ra, which indicates an energy-containing length scale $\sim$ 10 km for Earth (see §1).

The fact that the linear variation of Ra_ℓ with Λ demarcates the boundary between dipolar and multipolar states is evident by traversing the sections 1 and 2 marked on the Ra_ℓ line from left to right (figure 15(b)). In practice, this is done by following the evolution of the dynamo from a small seed field. Figure 16(a) shows the section 1 within dashed vertical lines, where $|\omega_M|$ crosses $|\omega_A|$. The variation of the dipole colatitude θ, shown in figure 16(b), indicates a multipolar field until this crossing, and a stable dipole thereafter. While the flow is predominantly made up of fast MAC waves of frequency $\omega \sim \omega_f$ before the transition, the slow waves of frequency $\omega \sim \omega_s$ are dominant after the transition (figures 16(c) & (d)). The multipole–dipole transitions are further evident in the contour plots of the radial magnetic field at the outer boundary, given in figure 17 for sections 1 and 2 marked in figure 15(b).

4. Concluding remarks

The present study investigates the dipole–multipole transition in rotating dynamos through the analysis of MHD wave motions. The limit of small Rossby number, based not only on the planetary core depth but also on the length scale of core convection, is considered. In this inertia-free limit, the dynamo polarity depends on the relative magnitudes of ω_M and ω_A, which in turn depend on the intensity of the self-generated field and the strength of buoyant forcing in the unstably stratified fluid layer. While the onset of slow magnetostrophic waves for $|\omega_M| \sim |\omega_A|$ is

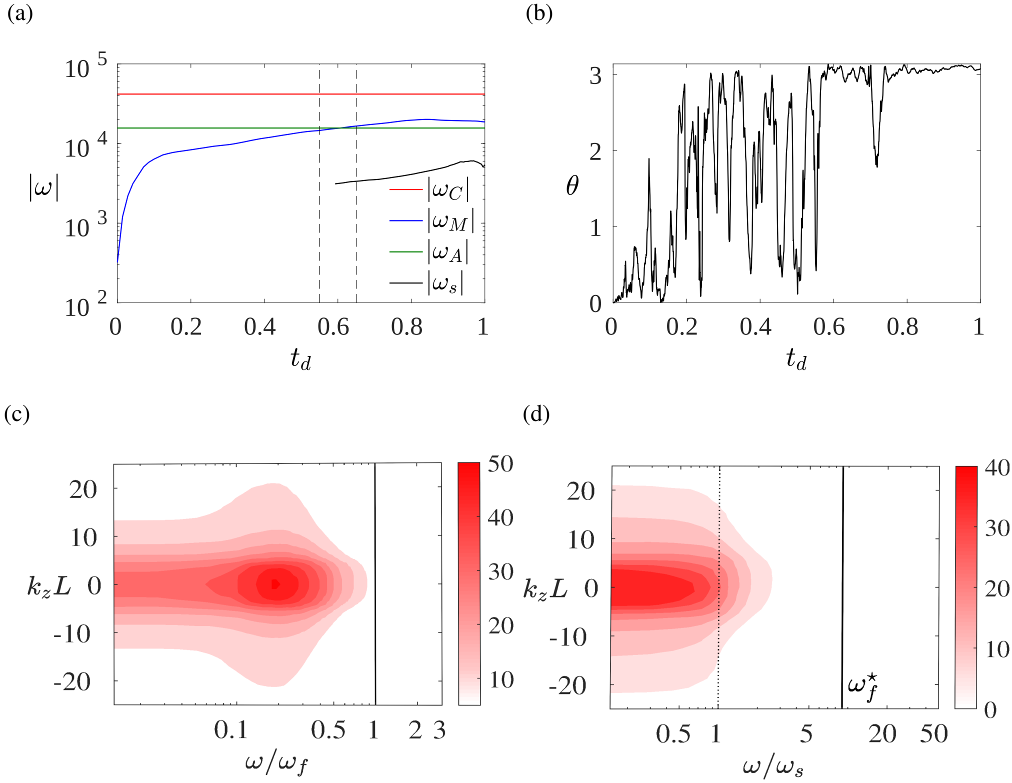

Figure 16: (a) Evolution the dynamo frequencies in a simulation beginning from a small seed magnetic field at $E = 1.2 \times 10^{-5}$, $Pm = Pr = 1$, $Ra = 4000$. The two dashed vertical lines at $t_d = 0.55$ and $t_d = 0.66$ represent the end points of section 1 marked in figure 15(b) with peak Elsasser numbers $\Lambda = 32$ and 56 respectively. (b) Evolution of the dipole colatitude in the above simulation. (c) & (d) FFT spectra of $\partial u_z/\partial t$ at cylindrical radius $s = 1$ for the scales $l \leqslant l_E$ at $\Lambda = 32$ and 56 respectively. The spectra are computed at discrete ϕ points and then averaged azimuthally. In (d), $\omega_f^* = \omega_f/\omega_s$, where ω_f and ω_s are the estimated fast and slow MAC wave frequencies.

known to produce the axial dipole from a chaotic multipolar state (see figures 16(b) & 17, as well as Varma & Sreenivasan (2022)), the annihilation of the slow waves for the same condition leads to the collapse of the axial dipole in strongly driven dynamos (see figures 12(c) & (d)). Since the appearance and disappearance of the slow waves are dynamically similar phenomena, the local Rayleigh number Ra_ℓ representing them fall on the same line that separates the dipolar and multipolar states. The variation of Ra_ℓ with the Elsasser number Λ is very similar in the linear magnetoconvection and dynamo models, which is remarkable given that the Alfvén frequency ω_M is determined by the imposed field in the linear model and by the self-generated field in the dynamo model.

The self-similarity of polarity reversals in the inertia-free regime can place a useful constraint on the Rayleigh number that admits reversals in the Earth. For $Ra_\ell \sim 10^4$, the classical Rayleigh number $R = Ra/E \sim 10^{17}$, taking a turbulent viscosity $\nu \approx \eta$ and a plausible ratio of core depth to the convective length scale, $L/\delta \sim 10^2$. This estimate, however, ignores the effect of double-diffusive convection, wherein compositional buoyancy is dominant and thermal buoyancy via secular cooling may contribute to about a fifth of the total forcing (Lister & Buffett 1995). For a given rotation rate, thermochemical convection increases $|\omega_M|$ through enhanced field

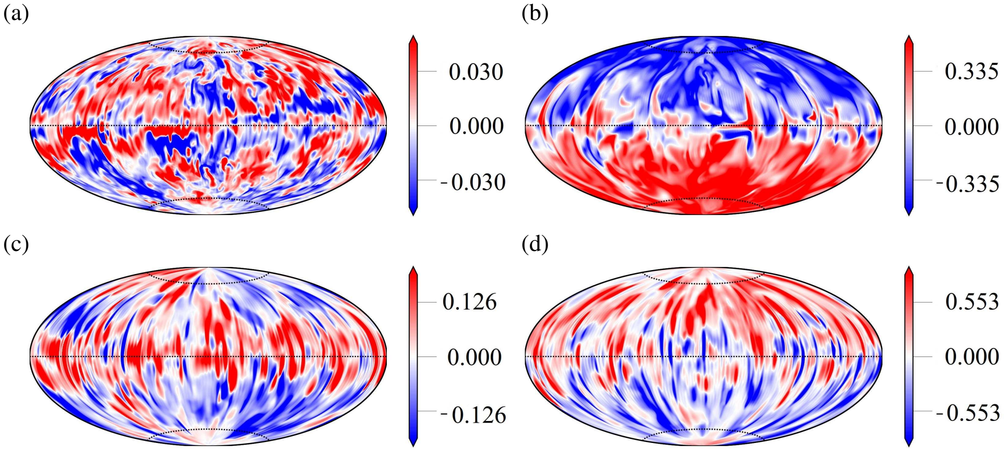

Figure 17: Shaded contours of the radial magnetic field at the outer boundary in two dynamo simulations. (a) and (b): $Ra_\ell = 2505$, corresponding to section 1 in figure 15(b), at $\Lambda = 32$ and 56 respectively. The dynamo parameters are $E = 1.2 \times 10^{-5}$, $Ra = 4000$, $Pm = Pr = 1$. (c) and (d): $Ra_\ell = 11740$, corresponding to section 2 in figure 15(b), at $\Lambda = 187$ and 216 respectively. The dynamo parameters are $E = 6 \times 10^{-5}$, $Ra = 18000$, $Pm = Pr = 5$.

generation, thereby pushing the value of Ra for reversals higher. On the other hand, Earth's core is believed to convect in response to large lateral variations in lower-mantle heat flux (e.g. Olson *et al.* 2015; Mound *et al.* 2019), which decreases the mean wavenumber $\bar{m}$ of the energy-containing scales. Consequently, $|\omega_M| \propto |B_\phi|\bar{m}$ decreases, thereby lowering the value of Ra for reversals. Our understanding of the convective regime for polarity reversals is far from complete, but the idea that polarity transitions are self-similar would eventually lead to improved parameter constraints for reversals.

Acknowledgments

This study was supported by Research Grant MoE-STARS/STARS-1/504 under Scheme for Transformational and Advanced Research in Sciences awarded by the Ministry of Education, India. DM's doctoral studentship is granted by the Council of Scientific and Industrial Research, India. The computations were performed on SahasraT, the Cray XC-40 supercomputer at IISc, Bengaluru.

REFERENCES

BRAGINSKY, S. I. 1967 Magnetic waves in the Earth's core. *Geomagn. Aeron.* **7**, 851–859.

BRAGINSKY, S. I. & ROBERTS, P. H. 1995 Equations governing convection in Earth's core and the geodynamo. *Geophys. Astrophys. Fluid Dyn.* **79**, 1–97.

BUFFETT, B. A. & BLOXHAM, J 2002 Energetics of numerical geodynamo models. *Geophys. J. Int.* **149** (1), 211–224.

BUSSE, F., DORMY, E., SIMITEV, R. & SOWARD, A. 2007 Dynamics of rotating fluids. In *Mathematical Aspects of Natural Dynamos* (ed. E. Dormy & A. M. Soward), *The Fluid Mechanics of Astrophysics and Geophysics*, vol. 13, pp. 160–163. CRC Press.

CHRISTENSEN, U. R. & AUBERT, J. 2006 Scaling properties of convection-driven dynamos in rotating spherical shells and application to planetary magnetic fields. *Geophys. J. Int.* **166** (1), 97–114.

DAVIDSON, P. A., STAPLEHURST, P. J. & DALZIEL, S. B. 2006 On the evolution of eddies in a rapidly rotating system. *J. Fluid Mech.* **557**, 135–144.

DORMY, E. 2016 Strong-field spherical dynamos. *J. Fluid Mech.* **789**, 500–513.

GLATZMAIER, G. A. & ROBERTS, P. H. 1995*a* A three-dimensional convective dynamo solution with rotating and finitely conducting inner core and mantle. *Phys. Earth Planet. Inter.* **91** (1-3), 63–75.

GLATZMAIER, G. A. & ROBERTS, P. H. 1995*b* A three-dimensional self-consistent computer simulation of a geomagnetic field reversal. *Nature* **377**, 203–209.

GUBBINS, D. 1999 The distinction between geomagnetic excursions and reversals. *Geophys. J. Int.* **137** (1), F1–F3.

KUTZNER, C. & CHRISTENSEN, U. R. 2002 From stable dipolar towards reversing numerical dynamos. *Phys. Earth Planet. Inter.* **131** (1), 29–45.

LISTER, J. & BUFFETT, B. A. 1995 The strength and efficiency of thermal and compositional convection in the geodynamo. *Phys. Earth Planet. Inter.* **91**, 17–30.

LOPER, D. E., CHULLIAT, A. & SHIMIZU, H. 2003 Buoyancy-driven perturbations in a rapidly rotating, electrically conducting fluid: Part I – Flow and magnetic field. *Geophys. Astrophys. Fluid Dyn.* **97**, 429–469.

MCDERMOTT, B. R. & DAVIDSON, P. A. 2019 A physical conjecture for the dipolar–multipolar dynamo transition. *J. Fluid Mech.* **874**, 995–1020.

MERRILL, R. T. 2011 *Our Magnetic Earth: The Science of Geomagnetism*. University of Chicago Press.

MOFFATT, H. K. 1978 *Magnetic Field Generation in Electrically Conducting Fluids*. Cambridge University Press.

MOUND, J., DAVIES, C., ROST, S. & AURNOU, J. 2019 Regional stratification at the top of Earth's core due to core–mantle boundary heat flux variations. *Nat. Geosci.* **12** (7), 575–580.

OLSON, P., CHRISTENSEN, U. & GLATZMAIER, G. A 1999 Numerical modeling of the geodynamo: mechanisms of field generation and equilibration. *J. Geophs. Res. Solid Earth* **104** (B5), 10383–10404.

OLSON, P. & CHRISTENSEN, U. R 2006 Dipole moment scaling for convection-driven planetary dynamos. *Earth Planet. Sci. Lett.* **250** (3-4), 561–571.

OLSON, P., DEGUEN, R., RUDOLPH, M.L. & ZHONG, S. 2015 Core evolution driven by mantle global circulation. *Phys. Earth Planet. Inter.* **243**, 44–55.

OLSON, P., DRISCOLL, P. & AMIT, H. 2009 Dipole collapse and rever- sal precursors in a numerical dynamo. *Phys. Earth Planet. Inter.* **173**, 121–140.

RANJAN, A, DAVIDSON, P. A., CHRISTENSEN, U. R. & WICHT, J. 2020 On the generation and segregation of helicity in geodynamo simulations. *Geophys. J. Int.* **221** (2), 741–757.

SALHI, A., BAKLOUTI, F. S., GODEFERD, F., LEHNER, T. & CAMBON, C. 2017 Energy partition, scale by scale, in magnetic Archimedes Coriolis weak wave turbulence. *Phys. Rev. E* **95** (2), 023112.

SARSON, G. R. & JONES, C. A. 1999 A convection driven geodynamo reversal model. *Phys. Earth Planet. Inter.* **111** (1-2), 3–20.

SODERLUND, K. M., KING, E. M. & AURNOU, J. M. 2012 The influence of magnetic fields in planetary dynamo models. *Earth Planet. Sci. Lett.* **333**, 9–20.

SREENIVASAN, B. & JONES, C. A. 2011 Helicity generation and subcritical behaviour in rapidly rotating dynamos. *J. Fluid Mech.* **688**, 5.

SREENIVASAN, B. & MAURYA, G. 2021 Evolution of forced magnetohydrodynamic waves in a stratified fluid. *J. Fluid Mech.* **922**.

SREENIVASAN, B. & NARASIMHAN, G. 2017 Damping of magnetohydrodynamic waves in a rotating fluid. *J. Fluid Mech.* **828**, 867–905.

SREENIVASAN, B., SAHOO, S. & DHAMA, G. 2014 The role of buoyancy in polarity reversals of the geodynamo. *Geophys. J. Int.* **199** (3), 1698–1708.

STARCHENKO, S. & JONES, C. A. 2002 Typical velocities and magnetic fields in planetary interiors. *Icarus* **157**, 426–435.

TEED, R. J., JONES, C. A. & TOBIAS, S. M. 2015 The transition to Earth-like torsional oscillations in magnetoconvection simulations. *Earth Planet. Sci. Lett.* **419**, 22–31.

VALET, J-P., MEYNADIER, L. & GUYODO, Y. 2005 Geomagnetic dipole strength and reversal rate over the past two million years. *Nature* **435** (7043), 802–805.

VARMA, A. & SREENIVASAN, B. 2022 The role of slow magnetostrophic waves in the formation of the axial dipole in planetary dynamos. *Phys. Earth Planet. Inter.* **333**, 106944.

WICHT, J. & OLSON, P. 2004 A detailed study of the polarity reversal mechanism in a numerical dynamo model. *Geochem. Geophys. Geosyst.* **5** (3).

WILLIS, A. P., SREENIVASAN, B. & GUBBINS, D. 2007 Thermal core-mantle interaction: Exploring regimes for 'locked' dynamo action. *Phys. Earth Planet. Inter.* **165**, 83–92.

ZAIRE, B., JOUVE, L., GASTINE, T., DONATI, J. F., MORIN, J., LANDIN, N. & FOLSOM, C. P. 2022 Transition from multipolar to dipolar dynamos in stratified systems. *Mon. Not. R. Astron. Soc.* **517** (3), 3392–3406.